AUTHOR

Akhrass Hussein, Conway James RW, Kronqvist Pauliina, Kallionpää Roosa E, Oliveira-Ferrer Leticia, Cervero Pasquale, Linder Stefan, Aepfelbacher Martin, Zauber Henrik, Rae James, Parton Robert G, Disanza Andrea, Scita Giorgio, Mayor Satyajit, Selbach Matthias, Veltel Stefan, Ivaska Johanna

TITLE

Cargo-specific recruitment in clathrin- and dynamin-independent endocytosis

YEAR

2021, Oct. 06

DOI

https://doi.org/10.1038/s41556-021-00767-x

VERSION

Final draft (AAM)

CITATION

Moreno-Layseca, P., Jäntti, N.Z., Godbole, R. *et al.* Cargo-specific recruitment in clathrin- and dynamin-independent endocytosis. *Nat Cell Biol* **23,** 1073–1084 (2021). https://doi.org/10.1038/s41556-021-00767-x

Cargo-specific recruitment in clathrin- and dynamin-independent endocytosis

Paulina Moreno-Layseca[1,2], Niklas Z. Jäntti[1], Rashmi Godbole[3,4], Christian Sommer[5], Guillaume Jacquemet[1,6], Hussein Al-Akhrass[1], James R. W. Conway[1], Pauliina Kronqvist[7], Roosa E. Kallionpää[8], Leticia Oliveira-Ferrer[2], Pasquale Cervero[2], Stefan Linder[2], Martin Aepfelbacher[2], Henrik Zauber[5], James Rae[9], Robert G. Parton[9,10], Andrea Disanza[11], Giorgio Scita[11], Satyajit Mayor[3], Matthias Selbach[5], Stefan Veltel[2,12]*, Johanna Ivaska[1,13, 14]*

[1]Turku Bioscience Centre, University of Turku and Åbo Akademi University, FI-20520 Turku, Finland.

[2]University Medical Center Hamburg-Eppendorf (UKE), 20251 Hamburg, Germany.

[3]National Centre for Biological Science (TIFR), Bellary Road, Bangalore, 560065, India.

[4]The university of Trans-Disciplinary Health Sciences and Technology (TDU), Yelahanka, Bangalore, 560064, India.

[5]Max-Delbrück-Centrum für Molekulare Medizin (MDC), 13092 Berlin, Germany.

[6]Faculty of Science and Engineering, Cell Biology, Åbo Akademi University, 20520 Turku, Finland.

[7]Institute of Biomedicine, Faculty of Medicine, University of Turku, FI-20520 Turku, Finland.

[8]Auria Biobank, Turku University Hospital and University of Turku, FI-20520 Turku, Finland.

[9]Institute for Molecular Bioscience, University of Queensland, Brisbane, QLD, 4072, Australia

[10]Centre for Microscopy and Microanalysis, University of Queensland, Brisbane, QLD, 4072, Australia.

[11]IFOM, Fondazione Istituto FIRC di Oncologia Molecolare and University of Milan, Milan, 20139, Italy.

[12]Hochschule Bremen, City University of Applied Sciences, 28199 Bremen, Germany.

[13]Department of Life Sciences, University of Turku, FI-20520 Turku, Finland.

[14]InFLAMES Research Flagship Center, University of Turku

***Correspondence to:** Johanna.Ivaska@utu.fi; Stefan.Veltel@hs-bremen.de

Abstract:

Spatially controlled, cargo-specific endocytosis is essential for development, tissue homeostasis and cancer invasion. Unlike the cargo-specific clathrin-mediated endocytosis, the clathrin- and dynamin-independent endocytic pathway (CLIC-GEEC, CG-pathway) is considered a bulk internalization route for the fluid phase, glycosylated membrane proteins and lipids. While the core molecular players of CG-endocytosis have been recently defined, evidence of cargo-specific adaptors or selective uptake of proteins for the pathway are lacking. Here we identify the actin-binding protein Swiprosin-1 (Swip1, EFHD2) as a cargo-specific adaptor for CG-endocytosis. Swip1 couples active Rab21-associated integrins with key components of the CG-endocytic machinery: Arf1, IRSp53 and actin, and is critical for integrin endocytosis. Through this function, Swip1 supports integrin-dependent cancer cell migration and invasion and is a negative prognostic marker in breast cancer. Our results demonstrate a previously unknown cargo selectivity for the CG-pathway and a role for specific adaptors in recruitment into this endocytic route.

Endocytosis is a vital process involving the internalization of extracellular material and cell surface receptors. This controls various functions ranging from fluid-phase nutrient uptake and spatially and temporally regulated traffic of adhesion and growth factor receptors, to pathogen entry[1]. The predominant view is that the specificity of endocytosis is achieved through cargo-specific adaptors, as described for clathrin-mediated endocytosis (CME)[2,3]. This raises the possibility that as-yet unidentified cargo adaptor proteins could function as key gatekeepers for other endosomal routes.

The CG-pathway internalizes a major fraction of the extracellular fluid phase, glycosylphosphotidylinositol (GPI)-anchored proteins and other cell surface receptors, including nutrient transporters, ion channels and cell adhesion receptors[4,5], as well as bacterial and viral pathogens[4,6]. This occurs through high-capacity tubulovesicular membrane uptake carriers called CLICs (clathrin-independent carriers)[7,8]. CLICs are formed via the recruitment of Arf1, actin-binding BAR-domain protein IRSp53 and Arp2/3 to the membrane, followed by Cdc42 activation of IRSp53 and Arp2/3-mediated actin polymerization, presumptively resulting in the scission of CLICs and generation of CG endosomes[9]. Although the core machinery of CG-endocytosis has been defined, no cargo-specific adaptors are known[10].

The small GTPase Rab21 binds directly to integrins to regulate endo/exosomal traffic, cytokinesis, chromosome integrity, endosomal signaling and anoikis[11–14]. Rab21 interacts with integrins independently of its activation state (GDP/GTP); nevertheless, integrin endocytosis requires Rab21 activity, but the exact mechanism is currently unknown[11]. In addition, very few Rab21 interactors have been identified[15].

Here, we identify Swip1 (EFHD2) as an interactor of Rab21 and a cargo-specific adaptor for CG-endocytosis.

Results:

Swip1 interacts with Rab21 and β1-integrin.

To identify Rab21-interacting proteins, we performed proteomic analyses by stable isotope labelling with amino acids in cell culture (SILAC) of Rab21 wild-type (WT), $Rab21^{Q76L}$ active mutant (CA-Rab21) or $Rab21^{T31N}$ inactive mutant (DN-Rab21) expressing cells[16,17]. This mass spectrometry (MS) strategy identified the actin-binding protein Swip1 as a putative active Rab21 interactor (Fig. 1a, Extended Data Fig. 1a-d, Supplementary Table 1). GFP pulldowns from cell lysate demonstrated endogenous Swip1 binding preferably to WT and CA-Rab21, and not to the closely related Rab5 GTPase (Fig. 1b, Extended Data Fig. 1e). Moreover, purified recombinant GST-Swip1 interacted directly with GTP-analog loaded recombinant Rab21 (positive control: Rab21-GTP specific interactor APPL1[18,19] ; Fig. 1c). We next validated the interaction in cells, where Swip1 localized to GFP-Rab21-containing endosomes (Fig. 2a) and proximity ligation assay (PLA) indicated endogenous Swip1 and Rab21 association in intact cells (Fig. 2b). Rab21 localizes with membrane-proximal puncta and early endosomes positive for endocytosed active β1-integrins[11,14,20]. Concordantly, bimolecular fluorescence complementation (BiFC)[21] revealed Swip1 and Rab21 interaction in structures overlapping predominantly with EEA1, Rab5 and VPS35 and to a lesser extent with late endosome markers (Extended Data Fig. 2a-c). Furthermore, Swip1 localized to Rab21-positive, β1-integrin-containing endosomes (Extended Data Fig. 3a). These data indicate that Swip1 interacts with integrin-associated Rab21 in cells.

Total internal reflection fluorescence (TIRF) microscopy of endocytic events on the plasma membrane revealed V1-Rab21/V2-Swip1 complexes moving at the cell-ECM interface in live cells[9,22] (Fig. 2c). The BiFC interaction puncta were dynamic, detected at the cell periphery and in the cell center, and were absent in Venus-expressing control cells (Supplementary Video 1). Structured illumination microscopy (SIM) images of the cell-ECM

interface revealed that Swip1, Rab21 and β1-integrin-positive structures extended vertically into the cell (Fig. 2d-e, x-z projections, Extended Data Fig. 3b). In these structures, Swip1 co-localized significantly more with Rab21 than Rab5, Rab7 and Rab11 (Extended Data Fig. 3c), indicating a degree of specificity for Rab21 binding. Together, these data identify Swip1 as an interactor of active Rab21, overlapping with β1-integrins in endosomal compartments and in close proximity with the plasma membrane.

Swip1 associates with CG-pathway components

Interestingly, Arf1 was detected as an active Rab21 interactor alongside Swip1 (Fig. 1a, Extended Data Fig. 1a-d) prompting us to test whether Rab21 and/or Swip1 associate with Arf1. Arf1 is a known regulator of CG-endocytosis, where cargo uptake is mediated by tubulovesicular membrane invaginations[23]. Both GFP-Rab21 and GFP-Swip1 co-immunoprecipitated with endogenous Arf1 (Fig. 3a). In addition, another CG-endocytosis regulator, IRSp53[10], was also detected in the GFP-immunoprecipitations (Fig. 3a) and immunoprecipitation of endogenous IRSp53 co-precipitated endogenous Swip1 and Arf1 (Fig. 3b). Moreover, significant PLA signal between IRSp53 and active β1-integrin (12G10 active-integrin conformation-specific antibody) showed close proximity of the endogenous proteins (Fig. 3c). These data indicate that the Rab21-β1-integrin-Swip1 complex is associated with the CG-endocytosis machinery. To investigate this in more detail, we imaged Swip1 co-localization with known components of CME, caveolin-mediated endocytosis and CG-endocytosis using SIM. Swip1 co-localized significantly more with Rab21, Arf1 and IRSp53 than with clathrin, the clathrin adaptor AP2, caveolin or dynamin2 (Fig. 3d-e). These data are consistent with Rab21-mediated integrin endocytosis remaining unaffected by clathrin inhibition[12], the clathrin and caveolin endocytic pathway components not being enriched in the active Rab21 MS-fractions (Fig. 1a, Extended Data Fig. 1a-d) and with the absence of dynamin I/II in bimolecular complementation affinity purified (BiCAP)[21] V1-

Rab21 and V2-Swip1 complexes in cells (Fig. 3f). Furthermore, using another super-resolution microscopy technique DNA-PAINT[24] (Extended Data Fig. 4a) we detected ring-like structures of GFP-Swip1 co-localizing with Arf1-HA at the TIRF plane. Moreover, Rab21/Swip1-BiFC puncta were detected dynamically moving towards IRSp53-positive structures before disappearing from the TIRF plane in live cells (Fig. 3g, Supplementary Video 2). These data indicate the existence of a Swip1/Rab21-GTP complex that links to the CG-endocytosis machinery.

Swip1-regulated endocytosis of active β1-integrins is Rab21 dependent

We next investigated the requirement for Swip1 for integrin endocytosis. Silencing of Swip1 decreased the uptake of cell surface-labelled active β1-integrin in MDA-MB-231 cells. Swip1 silencing-induced inhibition of integrin endocytosis was apparent at the 5-minute time point and persisted for up to 30 minutes (Fig. 4a). Ectopic expression of RNAi-resistant GFP-Swip1 rescued β1-integrin endocytosis in Swip1-silenced cells and increased the uptake in control siRNA-transfected cells (Fig. 4b). Reduced integrin uptake was specifically due to Swip1 silencing and not lower integrin levels, as evidenced by total β1-integrin protein levels remaining unaffected by Swip1 silencing, along with surface levels of total, active and inactive β1-integrins (Extended Data Fig. 4b-c). We then asked whether the Rab21-Swip1 complex could discriminate between active and inactive β1-integrins. Internalization of inactive β1-integrin (Mab13 antibody) was unaffected by Swip1 or Rab21 silencing (Fig. 4c). These data are in line with previous reports of active β1-integrins signaling from Rab21 endosomes[14] and Rab21-integrin interaction requiring the conserved KR-residues within the integrin α-subunit cytoplasmic tail GFFKR-motif[11]. Thus, this process potentially interferes with conserved salt bridge interactions (between α-subunit R and the conserved acidic

145 residue of the β-cytoplasmic domain) known to stabilize integrins in their inactive
146 conformation[25].

147 To assess the impact of Rab21 in Swip1-mediated recruitment of integrins, we mutated the
148 key Rab21-interacting residues (KR1160/61AA) in the integrin α2-subunit[11,14]. This
149 significantly reduced integrin co-localization with Swip1-positive structures (Fig. 4d).
150 Furthermore, colocalization of β1-integrin with Swip1 was reduced in Rab21-silenced cells
151 (Fig. 4e); indicating that a preserved integrin-Rab21 interaction is required for Swip1-
152 mediated recruitment of the integrin receptor. In line with Rab21 interacting with multiple
153 integrin α-subunits[11], we found that Swip1 and Rab21 co-precipitated with several distinct
154 GFP-tagged integrin α-subunits (Fig. 4f). Importantly, Swip1 silencing decreased the
155 internalization of β1-integrin and several different α-subunits (Fig. 4g and Extended Data
156 Fig. 4d). Inhibition of receptor recycling with primaquine further amplified the difference in
157 integrin internalization between control- and Swip1-silenced cells (Fig. 4g and Extended Data
158 Fig. 4d). This indicates that Swip1 regulates integrin traffic at the step of internalization,
159 where it specifically regulates endocytosis of Rab21-bound active integrins.

160

161 **Swip1 regulates integrin uptake via the CG-pathway**

162 To explore the role of the CG-pathway in Swip1-mediated endocytosis, we silenced Arf1 and
163 IRSp53, both essential members of the CG-pathway, with two independent siRNAs. This
164 significantly decreased β1-integrin endocytosis in MDA-MB-231 cells (Extended Data Fig.
165 5a). Furthermore, integrin endocytosis was impaired in IRSp53-null mouse embryonic
166 fibroblasts (IRSp53−/− MEF; Extended Data Fig. 5b). This was specifically due to reduced
167 integrin uptake and not due to lower integrin levels since total integrin levels were unaffected
168 by loss of IRSp53 (Extended Data Fig. 5b). Overexpression of ectopic GFP-Swip1
169 significantly increased integrin uptake (Extended Data Fig. 5c). This was dependent on the

CG-pathway machinery, as depletion of IRSp53 abolished GFP-Swip1 overexpression-induced β1-integrin endocytosis (Fig. 4h). The ability of ectopic Swip1 to augment β1-integrin endocytosis was most likely due to Swip1 overexpression-augmented recruitment of β1-integrins to IRSp53 (Fig. 4i, Extended Data Fig. 5d). Taken together, these data link Swip1 with β1-integrin endocytosis by the CG-pathway under basal conditions.

Swip1 is a cargo adaptor for the CG-pathway

CG-endocytosis is the major route for the bulk uptake/internalization of different kinds of cargo[5] whereas Rab21 has been primarily linked to integrin internalization[11]. To explore the possibility that β1-integrins enter the CG-pathway, we imaged the uptake of plasma membrane-labelled active β1-integrin with 10 kDa dextran; a fluid phase cargo for the CG-pathway. Immediately after endocytosis (2 and 5 minutes), integrins and dextran co-localized as clearly as dextran labelled with two different dyes (Fig. 5a). Moreover, a large proportion of active β1-integrin (around 50%) colocalized with endocytosed dextran, while around 20% colocalized with transferrin (Extended Data Fig. 5e), indicating that both CME- and CG-pathways are active and facilitate uptake of active integrins. To assess whether Swip1 is a cargo-adaptor or an integral member of the CG-pathway, we investigated if it regulates the endocytosis of other CG-cargos. Swip1 silencing had no effect on the uptake of 10 kDa dextran or MHCI (Fig. 5b-c). In contrast, silencing of IRSp53 significantly impaired endocytosis of both cargos, validating the approach. Similar data were obtained in two additional triple negative breast cancer cell lines MDA-MB-468 and BT-20, where Swip1 silencing significantly reduced β1-integrin uptake, but not MHCI uptake (Fig. 5d, Extended Data Fig. 6a). The effect on β1-integrin endocytosis was more prominent in the MDA-MB-468 cells, which express higher endogenous Swip1 than the BT-20 cells (Extended Data Fig. 6b). Furthermore, Swip1 depletion did not affect the endocytosis of transferrin or EGFR (Extended Data Fig. 6c-d), which are internalized through CME or dynamin-dependent non-

196 clathrin endocytosis[26,27]. Thus, Swip1 regulates endocytosis of β1-integrin, but not of other
197 CG cargos, indicative of a role for Swip1 as an integrin-specific CG-cargo adaptor.

198 The CG-pathway responds specifically to transient changes in cell membrane tension.
199 Constitutive activity of the pathway is augmented following a strain relaxation, such as
200 shifting cells from hypotonic to isotonic medium leading to a decrease in membrane
201 tension[28]. Treatment of cells with hypotonic medium followed by a shift to isotonic medium,
202 significantly increased uptake of 10 kDa dextran and β1-integrin, as compared to the cells in
203 isotonic medium. While dextran-uptake was elevated similarly in control- and Swip1-
204 silenced cells, when cells were shifted from hypotonic to isotonic medium, β1-integrin uptake
205 did not increase by this treatment in the Swip1-silenced cells, in line with the notion of Swip1
206 facilitating specifically β1-integrin uptake through the CG-pathway (Fig. 5e, Extended Data
207 Fig. 7a). This observation further confirmed β1-integrin as a Swip1 recruited cargo for the
208 CG-pathway.

209

210 **Swip1 associates with Arf1 to direct integrin cargo towards CG-endocytosis**

211 To investigate the mechanism through which Swip1 provides cargo-specificity to the CG-
212 pathway, we silenced Rab21 and assessed the colocalization of the CG-pathway component
213 IRSp53. After Rab21 silencing, colocalization of IRSp53 with Swip1 was significantly
214 reduced, indicating that recruitment of Swip1 to the CG-pathway is dependent on binding to
215 Rab21 and β1-integrin (Fig. 5f). Swip1 did not interact directly with IRSp53, while IRSp53
216 still associated with VASP, a known IRSp53 interactor[29–31] (Extended Data Fig. 7b-c). Next,
217 we explored the possible link between Swip1 and Arf1. Unexpectedly, we found that Swip1
218 associates preferentially and specifically with the inactive mutant ($Arf1^{T31N}$), but not the
219 active Arf1 ($Arf1^{Q71L}$; Fig. 5g). Arf1 localization at the plasma membrane precedes the
220 formation of CG endocytic tubules, and its activation is required for CG-endocytosis[9,32].

Since Swip1 is not activating the CG-pathway, nor an integral part of it, we propose a model where Swip1 targets Rab21-bound integrins to the CG-pathway as a pre-assembled module with inactive Arf1, which is then recruited to the endocytic CG-machinery.

Cumulatively, these data imply that Swip1 specifically directs integrin cargo towards CG-endocytosis, rather than affecting the overall activity of this pathway. These data help to explain the long-standing conundrum whereby active Rab21 is required for integrin endocytosis, yet binds integrins in both GDP- and GTP-bound states[11]. Here we show that Swip1 interacts specifically with Rab21-GTP, coupling active Rab21 and integrin cargo to CG-endocytosis.

Integrin trafficking by the CG-pathway requires actin binding to Swip1

A common emerging theme among non-clathrin endocytosis is a reliance on the actin cytoskeleton[33]. Intrigued by the established actin-binding activity of Swip1[34], we investigated whether this function was important for Swip1-mediated integrin CG-endocytosis. Deleting the first EF-hand domain (EF1) rendered Swip1 unable to bind actin, concordant with a previous report[34], and abolished its ability to facilitate integrin endocytosis (Fig. 6a-c). In contrast, EF2 deletion had no significant effect on Swip1-induced integrin uptake. This indicates that Swip1 binding to actin is necessary for its ability to induce integrin endocytosis. SIM imaging revealed F-actin overlap with Swip1 and β1-integrin close to the cell-ECM interface (Fig. 6d), indicating that Swip1 and the actin cytoskeleton are in close proximity during integrin endocytosis.

In addition to Swip1 localization to cell-ECM-proximal structures, we observed Swip1 deeper inside the cell, where it overlapped with Rab21-positive endosome-like vesicles (Fig. 6e) and F-actin in discrete puncta around Rab21 vesicles (Fig. 6e yellow arrows, Supplementary Video 3). Similar localization was visualized using GBP-APEX

(GFP-binding protein soybean ascorbate peroxidase) labelled GFP-Swip1 imaged with electron microscopy (Fig. 6f)[35]. Swip1 localized to filaments close to the plasma membrane and in the vicinity of endosomes (Fig. 6e pink arrow and 6f blue arrows). Swip1 localization with actin on Rab21 endosomes led us to investigate whether Swip1 regulates endosome movement. Silencing of Swip1 significantly reduced the speed of GFP-Rab21 vesicles, but not vesicle number (Extended Data Fig. 7d), and restricted their subcellular distribution to the cell periphery (Fig. 6g, Supplementary Videos 4-5). The motility of Rab21 vesicles was actin-dependent, as the actin inhibitor cytochalasin D reduced vesicle speed (Fig. 6h), consistent with previous observations[11]. Furthermore, re-expression of WT-Swip1, but not the actin binding-deficient EF1-deleted-Swip1, fully restored vesicle speed (Fig. 6i, Extended Data Fig. 8a). Taken together, these data highlight a role for actin in both Swip1/Rab21-dependent integrin CG-endocytosis and Rab21-mediated integrin endosomal traffic within the cell (Fig. 6j).

Swip1 regulates adhesion turnover, migration and invasion

Integrin endocytosis and intracellular transport are crucial for integrin turnover, cell migration and invasion[15,36]. Concordant with this notion we found that vinculin-containing focal adhesions accumulated in Swip1-silenced cells on collagen-I-, fibronectin- and laminin-coated surfaces (Fig. 7a). This phenotype was also present in cells silenced for Arf1 or IRSp53 (Extended Data Fig. 8b), indicating that CG-endocytosis of integrins may regulate adhesion dynamics and cell motility. Using live-cell imaging of paxillin-positive focal adhesions, we observed significantly slower adhesion assembly and disassembly rates in Swip1-silenced cells compared to control cells (Fig. 7b). Furthermore, live imaging of BiFC Rab21-Swip1 complexes and paxillin revealed significant enrichment of BiFC signal in close proximity to focal adhesions, indicating that, at the ventral surface of the cell, the Swip1-

Rab21 interaction occurs preferentially in the vicinity of adhesion sites (Fig. 7c, Supplementary Video 6). Swip1 regulation of focal adhesions correlated with significantly impaired cell migration (Fig. 7d, Extended Data Fig. 8c), in line with previously reported migration defects of IRSp53-null fibroblasts[31]. Swip1 silencing also inhibited the migration speed of randomly migrating MDA-MB-231 and MDA-MB-468 cells (Extended Data Fig. 9) and MDA-MB-231 cell invasion through a 3D collagen matrix (Fig. 7e). These data indicate that Swip1 supports integrin adhesion dynamics, in concert with the migration and invasion of triple-negative breast cancer (TNBC) cells.

High levels of Swip1 are a negative prognostic factor in triple-negative breast cancer

To assess the clinical relevance of our findings, we analysed Swip1 expression in a cohort of human breast cancer samples. Quantitative PCR (qPCR) analyses of Swip1 mRNA levels from 192 breast cancer specimens revealed that Swip1 expression was significantly increased in the highest-grade tumors and the most metastatic breast cancer subtypes: HER2-positive (HER2+) and TNBC (Extended Data Fig. 10). These findings were further validated by immunohistochemistry of Swip1 in HER2+ and TNBC tissue microarrays (Extended Data Fig. 10b). Swip1 was highly expressed in a large proportion of both breast tumour subtypes (65-75%). However, only in the case of TNBC was high Swip1 staining associated with a poorer clinical outcome (Fig. 7f). Moreover, we found that patients with high membranal Swip1 expression had a more pronounced correlation with poor clinical outcome (Extended Data Fig. 10c-d). Importantly, the Cox proportional hazards model showed that high membranal Swip1 is associated with a poorer prognosis, after adjustment for Ki67-positivity, tumour size, lymph node metastasis or tumour grade (Extended Data Fig. 10d). Finally, we observed that TNBC patients with high membranal Swip1 had significantly more lymph node metastasis compared to medium-low membranal Swip1-expressing patients (Fisher's exact

test, p=0.037) (Extended Data Fig. 10e). These data demonstrate that elevated Swip1 levels strongly and independently correlate with breast cancer metastasis and reduced survival in TNBC. These findings support the use of Swip1 as a prognostic marker for TNBC and as a potential drug target for this clinically challenging breast cancer subtype.

Discussion

Swip1 has not been previously associated with endocytosis and evidence for specific cargo adaptors or selective uptake in the CG-endocytosis pathway has been lacking. Our findings place Swip1 as a validated cargo-specific adaptor for the CG-pathway. Swip1 directs active Rab21 and β1-integrins to the CG-pathway and is necessary for active integrin endocytosis through this route, while fully dispensable for the uptake of other CG-cargos. This demonstrates an important and unexpected feature of this pathway: cargo-specific adaptor-based recruitment of receptors. It also highlights the possibility of unprecedented cargo-selective functions for the CG-pathway in a manner similar to that described for numerous other endocytosed proteins following different endocytosis routes.

We find that IRSp53 is required for CG-pathway uptake of integrins and that this is important for efficient cell migration and invasion. This adds a pathway to the list of IRSp53-regulated cell migration and invasion mechanisms, including filopodia generation[29,37], membrane ruffling[38]and curvature sensing with WAVE at the neck of membrane invaginations[39]. Moreover, our findings shed light on previous studies demonstrating that Arf1 depletion results in defective adhesion and migration in MDA-MB-231 cells[40–42]. Integrin traffic is a key regulator of cell motility and adhesion dynamics in many different contexts[43–45]. We show that Arf1-depletion significantly inhibits integrin uptake and induces accumulation of large focal adhesions, similarly to Swip1 and IRSp53 silencing. These data link integrin uptake via the CG-pathway to regulation of cell adhesion. It has been shown that Arf1 is

recruited to the forming endocytic pit long before scission, and that Arf1 activation is a key regulatory step in promoting endocytosis via the CG-pathway[9,23]. Our observation that Swip1 associates with inactive Arf1 supports a model where inactive Arf1 associates with the Swip1-Rab21GTP-integrin complex and thereby concentrates the integrin cargo at the site of the forming pit. Subsequently, activation of Arf1 releases the cargo from its adaptor for association with actin, which persists during endocytosis through the CG-pathway.

Interestingly, knockout of *Swip-1* in *Drosophila* results in a mild adhesion defect similar to deletion of the Rho-GAP-domain-containing protein GRAF1, another regulator of CLIC formation, suggesting an *in vivo* relevant role for Swip1 in regulating cell-ECM interactions[32,46]. We find that Swip1 facilitates cancer cell migration *in vitro* and that high Swip1 correlates with increased cancer dissemination in patients, in line with Swip1 driving increased actin protrusion and migration in metastatic lung adenocarcinoma cells[47]. In macrophages, inflammatory shock-induced migration is Swip1-dependent[48,49], while Swip1 deletion in mice induces faster B-cell migration *in vivo*; suggesting cell type- and possibly migration mode-specific roles for Swip1[50]. Importantly, these studies focus on the role of Swip1 as an actin regulator and the potential role of integrin traffic was not investigated.

Here, we show that Swip1 acts as a cargo-specific adaptor that bridges the CG endocytic machinery to Rab21-bound integrins, and couples Rab21 endosomes and their motility in cells, to the actin cytoskeleton. This dual functionality of Swip1 regulates cell adhesion turnover, migration and invasion. Perhaps unsurprisingly, given the importance of these events in cancer progression, Swip1 expression has clinically relevant implications for TNBC. Thus, Swip1 and the mechanism of its interaction with Rab21 offer potentially exciting therapeutic targets for metastatic breast cancer.

Acknowledgments:

The authors acknowledge Euro-BioImaging (www.eurobioimaging.eu) for providing access to imaging technologies and services via the Finnish Advanced Light Microscopy Node (Turku, Finland). We thank P. Laasola, J. Siivonen and Anja Gödicke for technical assistance, the Ivaska lab for critical reading of the manuscript and H. Hamidi for editing of the manuscript. We thank Virgilio Faila, Bernd Zobiak and Markku Saari for help with the microscopes and Dirk Mielenz, Aymelt Itzen and Peter Jackson for providing reagents. The Cell Imaging and Cytometry core (Turku Bioscience Centre, University of Turku and Åbo Akademi University and Biocenter Finland), the Euro-BioImaging Finnish Node, the Electron Microscopy Unit and Histocore at the University of Turku and the UMIF (UKE Microscopy Imaging Facility, Universitätsklinikum Hamburg, Eppendorf) are acknowledged for services, instrumentation and expertise. This study has been supported by DFG (VE 750/2-1) and Alexander von Humboldt-Foundation (S.V.), ProExzellenzia Hamburg and Academy of Finland (321493 to P.M.L. 325464 to J.I.), an ERC CoG grant 615258 (J.I.); by grants and a fellowship from the National Health and Medical Research Council of Australia (grants APP1140064 and APP1150083 and fellowship APP1156489 to R.G.P.) and the Australian Research Council Centre of Excellence in Convergent Bio-Nano Science and Technology, CE140100036 (R.G.P.).

Author contributions:

Conceptualization, S.V. and J.I.; Methodology, P.M.L., N.Z.J., C.S., R.G., G.J., H.A., J.R.W.C., M.S., S.M., S.V., R.G.P., J.R. and J.I.; Formal Analysis, P.M.L., N.Z.J., C.S., R.G., G.J., P.K., R.E.K., L.O.F., H.Z., S.M., M.S., S.V. R.G.P., J.R. and J.I.; Investigation, S.V., P.M.L. and J.I.; Resources, P.C., S.L., M.A., G.S. and A.D.; Writing – Original Draft, P.M.L. and J.I.; Writing – Review and Editing, S.V., P.M.L., G.J., N.Z.J., J.R.W.C., R.G.P. and J.I.; Supervision, P.M.L., S.V. and J.I.; Funding Acquisition, S.V., M.A., P.M.L., R.G.P. and J.I.

Competing interests:

Authors declare no competing interests.

Figure legends:

Fig. 1. Swip1 (EFHD2) interacts directly with active Rab21.
(a) SILAC proteomics analysis of GFP-Trap pulldowns in MDA-MB-231 cells expressing GFP-CA-Rab21^{Q78L} (constitutively active GTP-bound Rab21) vs GFP alone. Plot shows mean fold-changes from forward and reverse experiments against absolute protein abundances (intensity-based absolute quantification, iBAQ). Abundance bins were defined by including 1000 proteins in a subsequent order. Log10 fold change of proteins were tested for statistical significance using double-sided significance B tests. No multiple hypothesis correction method was applied, due to the small number of selected proteins for the statistical analysis. Proteins with a *P*-value < 0.01 are represented by a triangle, while non-significant proteins are shown as circles. P-values are depicted in the figure for a selected set of proteins. Proteins in red are markedly enriched in the CA-Rab21 fraction and proteins in blue are known endosomal proteins clathrin (CLTA, CLTB, CLTC), AP2 (AP2A1, AP2B1, AP2M1, AP2S1), caveolin (CAV1) and dynamin II (DNM2), which are not specifically enriched. **(b)** Representative immunoblots of GFP-Trap pulldowns from MDA-MB-231 cells transfected with the indicated constructs and probed for GFP and for endogenous Swip1. GFP-DN-Rab21: Rab21^{T33N} dominant negative, GDP-bound/nucleotide-free (n = 3 independent experiments). **(c)** A Coomassie-stained gel and immunoblot of GST pulldowns with the indicated GST-tagged proteins and recombinant Rab21 bound to a non-hydrolysable

form of GTP (GppNHP; active Rab21), GDP or no nucleotide after EDTA treatment (nuc free). Rab21-effector GST-APPL1 is used as a positive control (n = 3 independent experiments).

Fig. 2. Swip1 interacts with Rab21 and β1-integrin.
(a) Representative MDA-MB-231 cell expressing GFP-Rab21 and immunostained for Swip1. Arrows point to regions of overlap between Swip1 and GFP-Rab21. Scale bar, 10 μm. Micrograph is representative of 2 independent experiments. **(b)** Endogenous Rab21 and Swip1 are in close proximity in MDA-MB-231 cells. A proximity ligation assay (PLA; green spots) with the indicated antibodies is quantified. Goat IgG was included as a negative control and nuclei were stained with DAPI. Scale bars, 20 μm (n = 3). Data are presented as mean values ± 95% CI. Statistical significance was assessed with two-sided Mann Whitney test. ****$P<0.0001$. Number of cells examined over 3 independent experiments: Rab21-IgG, 121 and Rab21-Swip1, 126. **(c)** Representative TIRF microscopy of live MDA-MB-231 cells expressing the BiFC constructs V1-Rab21 and V2-Swip1 or Venus alone as a control. Scale bars, 5 μm (main images) and 2 μm (insets). Representative pictures of 3 independent experiments are shown. **(d)** MDA-MB-231 cells expressing mScarlet-I-Swip1 and GFP-Rab21 imaged using SIM. Blue and yellow squares highlight the regions of interest (ROI) in x-y that are magnified in x-z projections. Scale bars, 5 μm (main image) and 1 μm (insets). **(e)** SIM x-z projections of MDA-MB-231 cells expressing mScarlet-I-Swip1, GFP-Rab21 and immunostained for β1-integrin were quantified for co-localization with mScarlet-I-Swip1. Each dot represents the co-localization fraction in one cell. Number of cells examined over 2 independent experiments: GFP-Rab21, 16 and β1-integrin, 22. Scale bar, 0.5 μm.

Fig. 3. Swip1 interacts with members of the CG pathway.
(a) Representative immunoblots of GFP-Trap pulldowns from HEK293 cells transfected as indicated and blotted for GFP, endogenous IRSp53, Arf1 and β1-integrin (n = 2 independent experiments). **(b)** Representative immunoprecipitation with control mouse IgG or anti-IRSp53 antibodies from MDA-MB-231 cell lysate probed for endogenous Swip1, IRSp53 and Arf1 (n=2 independent experiments). **(c)** PLA with indicated antibodies alone (negative controls) and together to assess colocalization. Number of analyzed cells over 2 independent experiments: 12G10 only, 12; IRSp53 only, 18; 12G10 + IRSp53; 28. Scale bars, 10 μm. **(d)** SIM x-z projections of MDA-MB-231 cells expressing mScarlet-I-Swip1 and GFP-IRSp53 or Arf1-GFP. Scale bars, 0.8 μm. **(e)** MDA-MB-231 cells expressing mScarlet-I-Swip1 and immunostained for endocytic adaptor proteins or transfected as indicated, imaged with SIM and quantified for co-localization with mScarlet-I-Swip1. Each dot represents the co-localization fraction in one cell. Data are mean values ± 95% CI. Statistical significance was assessed with two-sided Mann Whitney tests. ****$P<0.0001$, ns=not significant. Number of analyzed cells over 3 independent experiments: Rab21, 50; AP2, 50; caveolin, 50; clathrin, 55; GFP-Rab21, 63; GFP-dynamin2, 63; GFP-IRSp53, 53 and Arf1-GFP, 62. **(f)** Representative immunoblots of BiCAP pulldowns from MDA-MB-231 cells transiently transfected as indicated and blotted for GFP/Venus, endogenous IRSp53, dynamin I/II and β1-integrin (n = 2 independent experiments). The GFP antibody recognizes both V1-Rab21 and V2-Swip1 (see also Ext. Data Fig. 2b). **(g)** Representative TIRF microscopy BiFC images of live MDA-MB-231 cells expressing V1-Rab21+V2-Swip1 and mcherry-IRSp53. Yellow arrows point to V1-Rab21+V2-Swip1 puncta that travel towards mcherry-IRSp53 puncta and then disappear from the TIRF plane. Scale bar, 1 μm. Representative pictures of 2 independent experiments are shown.

Fig. 4. Swip1 mediates endocytosis of active integrins via the CG pathway.
(a) Representative micrographs of active β1-integrin internalization in control- and Swip1-silenced MDA-MB-231 cells and quantification at 5, 15 and 30 minutes. Representative immunoblot to validate Swip1 silencing. Scale bars, 30 μm. **(b)** Quantification of active β1-integrin internalization at 15 min in control- or Swip1-silenced MDA-MB-231 cells expressing GFP or GFP-Swip1. Representative immunoblots of cell lysates probed as indicated. **(c)** Representative micrographs and quantification of inactive β1-integrin internalization in control-, Swip1- and Rab21-silenced MDA-MB-231 cells. Scale bar, 10 μm. **(d)** SIM x-z projections of MDA-MB-231 cells expressing mScarlet-I-Swip1 and GFP-tagged α2-integrin-WT or mutant α2 integrin-AA (integrin cytoplasmic sequence and mutated residues are depicted). Co-localization of GFP-tagged proteins with mScarlet-I-Swip1 was quantified. Scale bars, 0.5 μm. **(e)** SIM x-z projections of control (siCTRL) or Rab21-silenced (siRab21) MDA-MB-231 cells expressing mScarlet-I-Swip1 and immunostained for β1-integrin. Scale bars, 0.5 μm. Co-localization between mScarlet-I-Swip1 and β1 integrin was quantified. **(f)** Representative immunoblots of GFP-Trap pulldowns from MDA-MB-231 cells transfected and blotted as indicated. **(g)** Quantification of cell surface biotinylated β1-integrin or α6-integrin internalization in Swip1-silenced MDA-

MB-231 cells after the indicated times in the presence or absence of 100 μM primaquine. Bar charts show data as mean values ± SEM. Statistical significance was assessed using multiple comparison t-tests for paired data, with post hoc Holm-Sidak method, alpha=5.000%. For β1-integrin, ***$P= 0.00934$, *$P= 0.02015$; for α6-integrin, *$P=0.02196$, **$P=0.04683$. n=3 biologically independent experiments. **(h)** Quantification of β1-integrin internalization in control- or IRSp53-silenced MDA-MB-231 cells expressing GFP or GFP-Swip1. Representative immunoblots of cell lysates probed as indicated. **(i)** Representative micrographs and quantification of PLA with the indicated antibodies in MDA-MB-231 cells expressing GFP or GFP-Swip1. Scale bars, 10 μm.

Immunoblots are representatives of 3 independent experiments and calnexin is included as a loading control. (a, b, f, h). Scatter dot plots show data as mean values ± 95% CI. Statistical significance was assessed with two-sided Mann Whitney tests. (b) *$P=0.0275$, **$P=0.0260$; (h) ***$P=0.0003$; (i) ***$P=0.0001$; (a-e, h) ****$P<0.0001$, ns=not significant. Number of analyzed cells over 3 independent experiments are indicated in the Statistics and Reproducibility section.

Fig. 5. Swip1 is a cargo adaptor for the CG pathway.

(a) Double uptake of fluorescently labelled 10 kDa dextran-TMR (tetramethylrhodamine) with either dextran-FITC or Alexa Fluor 488-conjugated anti-β1-integrin antibody (12G10) in MDA-MB-231 cells for the indicated times. Scale bars, 10 μm (main image) and 3 μm (inset). **(b)** Representative micrographs and quantification of dextran-TMR or anti-β1-integrin antibody (12G10 conjugated to Alexa Fluor 488) internalization in control-, Swip1- (siRNA#1 or #2) or IRSp53- (siRNA#1 or #2) silenced MDA-MB-231 at 15 min. Scale bars, 10 μm. **(c)** Representative micrographs and quantification of Major Histocompatibility Complex I (MHCI) internalization in control-, Swip1- (siRNA#1) or IRSp53- (siRNA#1) silenced MDA-MB-231 at 15 min. Scale bars, 10 μm. **(d)** Quantification of β1-integrin and MHCI internalization in control- or Swip1- (siRNA#1 or #2) silenced MDA-MB-468 and BT-20 cells at 15 min. **(e)** Quantification of anti-β1-integrin antibody (12G10 conjugated to Alexa Fluor 488) and 10 kDa TMR-Dextran uptake in steady state or after recovery from hypotonic shock in control and Swip1- (siRNA#1 or 2) silenced MDA-MB-231 cells. **(f)** SIM x-z projections of control (siCTRL) or Rab21-silenced (siRab21) MDA-MB-231 cells expressing mScarlet-I-Swip1 and immunostained for IRSp53. Colocalization between mScarlet-I-Swip1 and endogenous IRSp53 was quantified. Scale bars, 0.5μm. **(g)** Cell lysates from HEK293T cells transfected with HA-ARF1^{T31N} (inactive) or HA-ARF1^{Q71L} (active) were incubated with 2μM of recombinant purified GST or GST-Swip1. Inputs and *in vitro* pull downs (IVBs) were loaded on SDS PAGE, analyzed by Ponceau staining to detect GST or GST-Swip1, and subjected to Western Blot analysis with the indicated antibody. Representative of 3 independent experiments is shown.

In all plots, data are presented as mean values ± 95% CI. Statistical significance was assessed with two-sided Mann Whitney tests. *P* values calculated compared to siCTRL condition: (b) ***$P=0.0001$, **$P=0.0004$; (d) *$P=0.0137$, **$P=0.0007$, ***$P=0.0006$; (a-e) ****$P<0.0001$, ns=not significant. Number of analyzed cells over 3 independent experiments are indicated in the Statistics and Reproducibility section.

Fig. 6. Swip1-actin binding regulates integrin traffic. (a) Swip1 domains. EF: EF-hand domain containing a calcium-binding site (shown in gray). **(b)** Representative GFP-pulldowns of 2 independent experiments in HEK293 cells expressing GFP, GFP-Swip1, or the truncated versions of Swip1 and blotted as indicated. **(c)** Quantification of β1-integrin uptake at 15 min in MDA-MB-231 cells expressing either GFP, GFP-Swip1 or the truncated versions of Swip1. **(d)** SIM x-z projections of MDA-MB-231 cells expressing mScarlet-I-Swip1, immunostained for β1-integrin and labelled with phalloidin. Scale bar, 0.7 μm. **(e)** Representative SIM x-y image of MDA-MB-231 cells expressing mScarlet-I-Swip1 and GFP-Rab21 and labelled with phalloidin. White squares highlight ROIs. ROI1 is magnified. Yellow arrows point to Swip1 overlap with actin on Rab21-containing vesicles. Pink arrow indicates actin filaments in close proximity to the vesicle. Scale bars, 5 μm (main image) and 0.5 μm (insets). **(f)** Electron microscopy images of GFP-Swip1 visualized using GBP-APEX. Squares highlight ROIs, which are magnified. Arrows point to Swip1-APEX-positive patches adjacent to filament-like actin structures (blue arrows) or vesicles (orange arrows). Scale bars, 0.5 μm (top image), 0.2 μm (middle image), 0.2 μm (inset 1) and 0.1 μm (inset 2). **(g)** Average speed of Rab21 vesicles, per cell, close to the TIRF plane over 2 min. Representative tracks of Rab21 vesicles in a control or a Swip1-silenced cell and representative immunoblot validating Swip1 silencing are shown. Calnexin is included as a loading control. Scale bar, 5 μm. **(h)** Average speed of Rab21 vesicle movement per cell upon treatment with cytochalasin D. **(i)** Average speed of Rab21 vesicle movement per cell upon Swip1 silencing and rescue with mScarlet-I-Swip1 or mScarlet-I-ΔEF1**. (j)** Swip1 directs integrins to CG endocytosis.

Data in plots are presented as mean values ± 95% CI. Statistical significance was assessed with two-sided Mann Whitney tests: (c) **$P=0.0034$, *$P=0.0356$, (g) **$P=0.0005$, ***P=0.0003, (h) ***$P=0.0007$, (i) ****$P<0.0001$, (c, i) ns=not significant. Number of analyzed cells over 3 independent experiments: (c) GFP,

92; GFP-Swip1, 94; GFP-ΔEF1, 161 and GFP-ΔEF2, 101. (g) siCTRL, 31; siSwip1 siRNA #1, 33; siSwip1 siRNA #2, 39. (h) DMSO, 21 and Cytochalasin D, 18. (i) 33 cells per condition.

Fig. 7. Swip1 regulates adhesion dynamics, cell motility and breast cancer progression.
(a) Representative masks of vinculin-containing focal adhesions in control- or Swip1-silenced MDA-MB-231 cells on collagen I. Analysis of adhesion number and total adhesion area per cell on different ECM components. Scale bars, 10 µm. **(b)** Visualization of GFP□paxillin dynamics in control- and Swip1-silenced cells. Color scale represents focal adhesion localization over time. Assembly and disassembly rates are quantified. Scale bar, 10 µm. **(c)** Representative TIRF microscopy BiFC images of live MDA-MB-231 cells expressing V1-Rab21, V2-Swip1 and mKate2-paxillin. Plot shows the nearest distance between EFHD2-Rab21 puncta or randomly distributed puncta and paxillin-positive focal adhesion. Scale bars, 25 µm (main image) and 1 µm (inset). **(d)** Migration of control-, Swip1- or Rab21-silenced MDA-MB-231 cells. Quantification of the wound area coverage over time are shown. **(e)** Relative invasion through fibrillar collagen I of control- and Swip1-silenced MDA-MB-231 cells. **(f)** Representative images of Swip1 staining in samples of HER2+ and TNBC breast cancer tissue microarrays and quantification of the percentage of tumors with high, medium or low Swip1. Overall survival of 133 TNBC patients with high (red) or medium and low (blue) staining of Swip1. Hazard ratio (HR) was 1.84 (95% CI 1.05 to 3.23). Scale bars, 20 µm.

Box-plots display median and quartiles of the data. Mean is displayed as +. Whiskers display maxima and minima. Representative immunoblots validating silencing are from 3 independent experiments; calnexin is a loading control (a, b, d, e). Data are mean ± 95% CI (a) or mean ±SEM (b, d). Statistical significance was assessed with two-sided Mann Whitney tests (a, b, c, e) or multiple comparison t-tests with post hoc Holm-Sidak method (e). Number of analyzed cells over 3 independent experiments are indicated in Statistics and Reproducibility section. *P* values calculated compared to siCTRL condition: (a-c) ****$P<0.0001$, (a) Collagen ***$P=0.0005$, Fibronectin ***$P=0.0002$ for Swip1 siRNA #1 and ***$P=0.0007$ for siRNA #2, (d) siSwip1 siRNA #1, *$P=0.022118, 0.00148533, 0.00320197, 0.00598189, 0.00156902$; siSwip1 siRNA #2, **$P=0.00161506, 8.929064e-005, 0.000190115, 0.000316543, 0.000100846$; siRab21, *$P=0.0158582, 0.0101405, 0.00574356, 0.0240206, 0.0286109$ for 8, 12, 16 and 18 hours, respectively; (e) *$P=0.0418$, **$P=0.0055$.

References

1. Kaksonen, M. & Roux, A. Mechanisms of clathrin-mediated endocytosis. *Nat. Rev. Mol. Cell Biol.* **19**, 313–326 (2018).

2. Mettlen, M., Chen, P.-H., Srinivasan, S., Danuser, G. & Schmid, S. L. Regulation of Clathrin-Mediated Endocytosis. *Annu. Rev. Biochem.* **87**, 871–896 (2018).

3. Sanger, A., Hirst, J., Davies, A. K. & Robinson, M. S. Adaptor protein complexes and disease at a glance. *J. Cell Sci.* **132**, (2019).

4. Mayor, S., Parton, R. G. & Donaldson, J. G. Clathrin-independent pathways of endocytosis. *Cold Spring Harb. Perspect. Biol.* **6**, (2014).

5. Maldonado-Báez, L., Williamson, C. & Donaldson, J. G. Clathrin-independent endocytosis: a cargo-centric view. *Exp. Cell Res.* **319**, 2759–2769 (2013).

6. Ferreira, A. P. A. & Boucrot, E. Mechanisms of Carrier Formation during Clathrin-Independent Endocytosis. *Trends Cell Biol.* **28**, 188–200 (2018).

7. Kirkham, M. *et al.* Ultrastructural identification of uncoated caveolin-independent early endocytic vehicles. *J. Cell Biol.* **168**, 465–476 (2005).

8. Howes, M. T. *et al.* Clathrin-independent carriers form a high capacity endocytic sorting system at the leading edge of migrating cells. *J. Cell Biol.* **190**, 675–691 (2010).

9. Sathe, M. *et al.* Small GTPases and BAR domain proteins regulate branched actin polymerisation for clathrin and dynamin-independent endocytosis. *Nat. Commun.* **9**, 1835 (2018).

10. Thottacherry, J. J., Sathe, M., Prabhakara, C. & Mayor, S. Spoiled for Choice: Diverse Endocytic Pathways Function at the Cell Surface. *Annu. Rev. Cell Dev. Biol.* **35**, 55–84 (2019).

11. Pellinen, T. *et al.* Small GTPase Rab21 regulates cell adhesion and controls endosomal traffic of beta1-integrins. *J. Cell Biol.* **173**, 767–780 (2006).

12. Pellinen, T. *et al.* Integrin trafficking regulated by Rab21 is necessary for cytokinesis. *Dev. Cell* **15**, 371–385 (2008).

13. Högnäs, G. *et al.* Cytokinesis failure due to derailed integrin traffic induces aneuploidy and oncogenic transformation in vitro and in vivo. *Oncogene* **31**, 3597–3606 (2012).

14. Alanko, J. *et al.* Integrin endosomal signalling suppresses anoikis. *Nat. Cell Biol.* **17**, 1412–1421 (2015).

15. Moreno-Layseca, P., Icha, J., Hamidi, H. & Ivaska, J. Integrin trafficking in cells and tissues. *Nat. Cell Biol.* **21**, 122–132 (2019).

16. Meyer, K. & Selbach, M. Quantitative affinity purification mass spectrometry: a versatile technology to study protein-protein interactions. *Front. Genet.* **6**, 237 (2015).

17. Hubner, N. C. *et al.* Quantitative proteomics combined with BAC TransgeneOmics reveals in vivo protein interactions. *J. Cell Biol.* **189**, 739–754 (2010).

18. Jean, S. & Kiger, A. A. RAB21 Activity Assay Using GST-fused APPL1. *Bio-Protoc.* **6**, (2016).

19. Zhu, G. *et al.* Structure of the APPL1 BAR-PH domain and characterization of its interaction with Rab5. *EMBO J.* **26**, 3484–3493 (2007).

20. Del Olmo, T. *et al.* APEX2-mediated RAB proximity labeling identifies a role for RAB21 in clathrin-independent cargo sorting. *EMBO Rep.* **20**, (2019).

21. Croucher, D. R. *et al.* Bimolecular complementation affinity purification (BiCAP) reveals dimer-specific protein interactions for ERBB2 dimers. *Sci. Signal.* **9**, ra69 (2016).

22. Bhave, M. *et al.* Functional characterization of 67 endocytic accessory proteins using multiparametric quantitative analysis of CCP dynamics. *Proc. Natl. Acad. Sci. U. S. A.* **117**, 31591–31602 (2020).

23. Kumari, S. & Mayor, S. ARF1 is directly involved in dynamin-independent endocytosis. *Nat. Cell Biol.* **10**, 30–41 (2008).

24. Schnitzbauer, J., Strauss, M. T., Schlichthaerle, T., Schueder, F. & Jungmann, R. Super-resolution microscopy with DNA-PAINT. *Nat. Protoc.* **12**, 1198–1228 (2017).

25. Park, E. J., Yuki, Y., Kiyono, H. & Shimaoka, M. Structural basis of blocking integrin activation and deactivation for anti-inflammation. *J. Biomed. Sci.* **22**, 51 (2015).

26. Caldieri, G. *et al.* Reticulon 3-dependent ER-PM contact sites control EGFR nonclathrin endocytosis. *Science* **356**, 617–624 (2017).

27. McMahon, H. T. & Boucrot, E. Molecular mechanism and physiological functions of clathrin-mediated endocytosis. *Nat. Rev. Mol. Cell Biol.* **12**, 517–533 (2011).

28. Thottacherry, J. J. *et al.* Mechanochemical feedback control of dynamin independent endocytosis modulates membrane tension in adherent cells. *Nat. Commun.* **9**, 4217 (2018).

29. Krugmann, S. *et al.* Cdc42 induces filopodia by promoting the formation of an IRSp53:Mena complex. *Curr. Biol. CB* **11**, 1645–1655 (2001).

30. Vaggi, F. *et al.* The Eps8/IRSp53/VASP network differentially controls actin capping and bundling in filopodia formation. *PLoS Comput. Biol.* **7**, e1002088 (2011).

31. Disanza, A. *et al.* CDC42 switches IRSp53 from inhibition of actin growth to elongation by clustering of VASP. *EMBO J.* **32**, 2735–2750 (2013).

32. Lundmark, R. *et al.* The GTPase-activating protein GRAF1 regulates the CLIC/GEEC endocytic pathway. *Curr. Biol. CB* **18**, 1802–1808 (2008).

33. Hemalatha, A. & Mayor, S. Recent advances in clathrin-independent endocytosis. *F1000Research* **8**, (2019).

34. Park, K. R. *et al.* Structural implications of Ca2+-dependent actin-bundling function of human EFhd2/Swiprosin-1. *Sci. Rep.* **6**, (2016).

35. Ariotti, N. *et al.* Modular Detection of GFP-Labeled Proteins for Rapid Screening by Electron Microscopy in Cells and Organisms. *Dev. Cell* **35**, 513–525 (2015).

36. Paul, N. R., Jacquemet, G. & Caswell, P. T. Endocytic Trafficking of Integrins in Cell Migration. *Curr. Biol. CB* **25**, R1092-1105 (2015).

37. Lim, K. B. *et al.* The Cdc42 effector IRSp53 generates filopodia by coupling membrane protrusion with actin dynamics. *J. Biol. Chem.* **283**, 20454–20472 (2008).

38. Miki, H., Yamaguchi, H., Suetsugu, S. & Takenawa, T. IRSp53 is an essential intermediate between Rac and WAVE in the regulation of membrane ruffling. *Nature* **408**, 732–735 (2000).

39. Pipathsouk, A. *et al.* WAVE complex self-organization templates lamellipodial formation. *bioRxiv* 836585 (2019) doi:10.1101/836585.

40. Koronakis, V. *et al.* WAVE regulatory complex activation by cooperating GTPases Arf and Rac1. *Proc. Natl. Acad. Sci. U. S. A.* **108**, 14449–14454 (2011).

41. Schlienger, S., Ramirez, R. A. M. & Claing, A. ARF1 regulates adhesion of MDA-MB-231 invasive breast cancer cells through formation of focal adhesions. *Cell. Signal.* **27**, 403–415 (2015).

42. Norman, J. C. *et al.* ARF1 mediates paxillin recruitment to focal adhesions and potentiates Rho-stimulated stress fiber formation in intact and permeabilized Swiss 3T3 fibroblasts. *J. Cell Biol.* **143**, 1981–1995 (1998).

43. Shafaq-Zadah, M. *et al.* Persistent cell migration and adhesion rely on retrograde transport of β(1) integrin. *Nat. Cell Biol.* **18**, 54–64 (2016).

44. Ezratty, E. J., Bertaux, C., Marcantonio, E. E. & Gundersen, G. G. Clathrin mediates integrin endocytosis for focal adhesion disassembly in migrating cells. *J. Cell Biol.* **187**, 733–747 (2009).

45. Sahgal, P. *et al.* GGA2 and RAB13 promote activity-dependent β1-integrin recycling. *J. Cell Sci.* **132**, jcs233387 (2019).

46. Hornbruch-Freitag, C., Griemert, B., Buttgereit, D. & Renkawitz-Pohl, R. Drosophila Swiprosin-1/EFHD2 accumulates at the prefusion complex stage during Drosophila myoblast fusion. *J. Cell Sci.* **124**, 3266–3278 (2011).

47. Fan, C.-C. *et al.* EFHD2 promotes epithelial-to-mesenchymal transition and correlates with postsurgical recurrence of stage I lung adenocarcinoma. *Sci. Rep.* **7**, 14617 (2017).

48. Zhang, S. *et al.* Swiprosin-1 deficiency impairs macrophage immune response of septic mice. *JCI Insight* **3**, (2018).

49. Tu, Y. *et al.* EFhd2/swiprosin-1 regulates LPS-induced macrophage recruitment via enhancing actin polymerization and cell migration. *Int. Immunopharmacol.* **55**, 263–271 (2018).

50. Reimer, D. *et al.* B Cell Speed and B-FDC Contacts in Germinal Centers Determine Plasma Cell Output via Swiprosin-1/EFhd2. *Cell Rep.* **32**, 108030 (2020).

Methods

Our research complies with all relevant ethical regulations; the use of the patient samples was approved by the Auria Biobank steering committee, University of Turku and the hospital district of South West Finland. Approval number AB19-4522.

Cell culture, cell transfection and ECM coatings

MDA-MB-231 and MDA-MB-468 (triple-negative human breast adenocarcinoma) cells were grown in Dulbecco's Modified Eagle's medium (DMEM) supplemented with 10 % fetal calf serum (FCS) and 1 % L-glutamine. BT-20 (triple-negative human breast adenocarcinoma) cells were grown in Eagle's Minimum Essential Medium supplemented with 10 % FCS and 1 % L-glutamine. Cells were purchased from the American Type Culture Collection (ATCC) and were routinely monitored for mycoplasma contamination (Catalogue numbers: MDA-MB-231, HTB-26; MDA-MB-468, HTB-132 and BT-20, HTB-19). Mouse embryonic fibroblasts (MEFs) [31] were cultured in DMEM supplemented with 20% FCS, 1% L-glutamine and 1 μg/ml puromycin. Human embryonic kidney 293 (HEK293, ATCC catalogue number CRL-1573) cells were cultured in DMEM supplemented with 20% FCS and 1% L-glutamine. No commonly misidentified cell lines were used for this study. MDA-MB-231 was authenticated by the German Collection of Microorganisms and Cell Cultures GmbH, using STR profiling and PCR assays to test the presence of mitochondrial DNA sequences from rodent cells such as mouse, rat, Chinese and Syrian hamster. The other cell lines used in the study were not authenticated. Plasmids of interest were transfected using Lipofectamine 3000 (Thermo Fisher Scientific) or jetPRIME® (Polyplus transfection) according to the manufacturer's instructions. The expression of proteins of interest was suppressed using 27 nM siRNA and lipofectamine siRNA Max (ThermoFisher Scientific) according to manufacturer's instructions. The siRNA used as control (siCTRL) was Allstars negative control siRNA (Qiagen, Cat. No. 1027281). The siRNA oligonucleotides targeting Swiprosin-1 (Swip1) were purchased from Sigma (siRNA #1 Cat. No. SASI_Hs01_00186848 and siRNA #2 Cat. No. SASI_Hs01_00186847). The siRNA oligonucleotides targeting Arf1 and IRSp53 were purchased from Qiagen (siARF1#1,Hs_BCAR1_5 FlexiTube siRNA, Cat. No. SI02757734; siBCAR1#6, Hs_BCAR1_6 FlexiTube siRNA, Cat. No. SI02757741). Coverslips were coated with either 10 μg/mL of fibronectin (FC010 Sigma), 12 μg/mL of laminin-1 (L4544 Sigma) or 300 μg/mL of collagen I from rat-tail (08-115 Sigma).

Plasmids

Human Rab21 (aa 16-225) constructs were cloned into a Gateway destination vector pgLAP1 (Addgene plasmid # 19702) to express Rab21 with an N-terminal GFP followed by a TEV cleavage site and an S-Tag in mammalian cells. As entry vector, we used pCR8/GW/Topo (Thermo Fisher, USA), in which human Rab21 was cloned by TOPO cloning. The Rab21 mutants Q76L (active) and T33N (inactive) were introduced into the entry clone by site-directed mutagenesis. Mouse full-length Swip1, ΔEF1-Swip1 (deletion in the EF1 domain, aa 96-166) and ΔEF2-Swip1 (deletion at the EF2 domain, aa 134-159) were a kind gift from Dr. Dirk Mielenz (Division of Molecular Immunology, Nikolaus-Fiebiger-Centre, University of Erlangen-Nuremberg, Germany). The corresponding coding sequences were subcloned into the pEGFP-N1 backbone vector using the XhoI and EcoRI restriction sites. Full-length Swip1 was also subcloned by TOPO cloning into the Gateway vector pCR8/GW/Topo. Then, a LR clonase II reaction was performed to shuttle full-length Swip1 into pGEX-4T1. mScarlet-I-Swip1 was generated from the GFP-tagged construct by introducing the mScarlet-I sequence using the AgeI and MfeI restriction sites. To generate mScarlet-ΔEF1-Swip1, the ΔEF1-Swip1 fragment was PCR amplified from pEGFP-ΔEF1-Swip1 using the 5'-agatctcgaGATGGCCACGGACGAGTTGGC-3' and 5'-cggtggatcCATCTTGAACGTGGACTGCAGCTCCTTAAAGG-3' primers, which added N- and C-terminal sites for the XhoI and BamHI restriction enzymes respectively. This fragment was then ligated into the mScarlet-I-Swip1 vector backbone, after both were digested with XhoI and BamHI. Arf1-HA and Arf1-GFP were obtained from Addgene (plasmids #79409 and #49578). IRSp53-mcherry and IRSp53-GFP were generated by the Genome Biology Unit supported by HiLIFE and the Faculty of Medicine, University of Helsinki, and Biocenter Finland. pDEST-V1-Rab21 was generated by shuttling the human Rab21 sequence (pENTR201-hRab21,ORFeome Library; Genome Biology Unit supported by HiLIFE and the Faculty of Medicine, University of Helsinki, and Biocenter Finland) into the destination vector pDEST-V1-ORF (Addgene 73635). pDEST-Swip1-V2 was generated by performing a clonase reaction between pCR8/GW/Topo-Swip1 and pDEST-ORF-V2 (Addgene 73638). pEF.DEST51-mVenus was obtained from Addgene (plasmid #154899).

Antibodies

The antibodies used in this work are listed in Supplementary Table 2.

Generation of stable cell lines and SILAC-cell culture treatment

To generate stable GFP-Rab21 expressing mammalian cell lines, a FRT (Flp Recombination Target)-entry site was first introduced into MDA-MB-231 breast cancer cells using the Flp-In technology (Thermo Fisher, USA). Briefly, MDA-MB-231 cells were transfected with pFRT/lacZeo2 and stable clones were isolated using Zeocin as the selection marker (200 µg/ml). The resulting MDA-MB-231-FRT cell line was then co-transfected with the pgLAP1-Rab21 plasmid and pOG44 and stable clones were selected in 500 µg/ml Hygromycin-containing medium and tested for GFP-Rab21 expression. Stable MDA-MB-231-GFP-Rab21 cell lines were cultivated in heavy (Arg-10/Lys-8) or light SILAC-DMEM medium plus Hygromycin (200 µg/ml) for 12 days to ensure at least 10 replication cycles for efficient labelling. Hygromycin supplementation was omitted for the last two days before the co-IP experiment.

Screening for Rab21 interaction partners by GFP pulldown

Each mass spectrometry experiment consisted of a mixture of a GFP-pulldown in active GFP-Rab21 expressing MDA-MB-231 cells (WT or active Rab21 Q76L mutant) grown in heavy medium and a GFP-pulldown in control cells (expressing GFP or inactive GFP-Rab21 T33N mutant) grown in light medium (forward experiment). In the reverse experiment, the heavy and light media were exchanged (label swap experiment). Briefly, co-IP samples were prepared as follows. Cells (two 15 cm dishes) were grown until 60-80% confluence, washed with ice cold PBSM (PBS + 5 mM $MgCl_2$), harvested in PBSM, pooled and washed again. Cell pellets were resuspended in 600 µl lysis buffer LB (50 mM Tris, pH 7.5, 5 mM $MgCl_2$, 150 mM KCl, 1.3% n-beta-octyl-D-glucopyranoside, 10 % Glycerol, protease and phosphatase inhibitors and 500 µM GppNHp for GFP-active Rab21-expressing cells or 500 µM GDP for GFP-inactive Rab21-expressing cells) and lysed by douncing 40x in a tissue grinder (dounce homogenizer) and incubating for 20 min on ice. The insoluble fraction was removed by centrifugation at 18000x g and the supernatant was incubated with 20 µl GFP-trap agarose beads (Chromotek) for 60 min at 4°C by overhead rotation. Beads were then washed three times with 500 µl washing buffer WB (50 mM Tris, pH 7.5, 5 mM $MgCl_2$, 300 mM KCl, 10 % Glycerol), combining the heavy, GFP-active Rab21 IP with the light, GFP-inactive Rab21 IP (forward experiment) during the second washing step. Proteins were eluted from the beads in 100 µl of U/T buffer (6 M urea, + 2 M thiourea in 10 mM HEPES, pH 8.0) for 15 min with shaking at 1400 rpm at room temperature. The eluted proteins were collected and the process repeated a second time to maximize protein yield. Eluted proteins were precipitated by adding 70 µl 2.5 M Na-Acetate, pH 5.0, 1 µl GlycoBlue (Thermo Fisher,

USA) and 1700 µl ethanol to the pooled elution fractions (200 µl) in a 2 ml tube. After an overnight incubation at 4°C, the precipitation mixture was centrifuged for 50 min at 20000x g and the resulting pellet dried for 15-20 min at 60-70°C.

For in-solution protein digestion we followed standard procedures [51]. Briefly, pellets were solubilized in U/T buffer, reduced with DTT, alkylated with iodoacetamide and digested by sequential addition of LysC (Wako) and Trypsin (Promega) overnight at room temperature. Peptides were desalted and stored on STAGE tips until LC-MS/MS analysis. Samples were analyzed using 240 min acetonitrile gradients on a 20 cm long 75 µm ID reversed phase column filled with 3 µm C18 beads (Dr. Maisch) using a Proxeon HPLC system (Thermo Fisher) coupled to the electrospray ion source of a Q Exactive Plus mass spectrometer (Thermo Fisher). The mass spectrometer was operated in the data dependent mode with a full scan (AGC target 3E6; R = 70,000) followed by up to ten MS2 scans (R = 17,500; maximal injection time 60 ms) and a dynamic exclusion for 30 sec. Raw files were analyzed using MaxQuant (version 1.5.2.8) using default parameters and searched against a Uniprot human protein database (2014-10).

For visualization purposes, all the identified proteins from each experiment were plotted (Fig. 1a, Extended Data Fig. 1a-d), where each spot corresponds to one identified protein by mass spectrometry. Each plot is representative of two independent experiments (forward and reverse, x- and y-axis), where every experiment consists of two independent IPs. The mean log2FCs from both experiments was plotted against absolute protein intensities (intensity-based absolute quantification, or iBAQ) and significance B was calculated according to Cox & Mann (2008) [52]. The error function was estimated using the erfc as is implemented in the pracma package [53], R package version 2.2.9. Abundance bins were defined by including 100 proteins in a subsequent order.

The proteomics data have been deposited to the ProteomeXchange Consortium via the PRIDE [54] partner repository with the dataset identifier PXD016478. The Log10 transformed ratios of the proteins identified by mass spectrometry are also available from the Supplementary Information (Supplementary Table 1).

Immunoprecipitations, BICAP and immunoblotting

MDA-MB-231 or HEK293 cells expressing GFP-tagged or split Venus-tagged (V1 or V2) proteins (one 10 cm dish per condition) were washed with cold PBS, harvested in PBS and pelleted. The cell pellet was resuspended in 200 µl of IP-lysis buffer (40 mM Hepes-NaOH,

75 mM NaCl, 2 mM EDTA, 1% NP40, protease and phosphatase inhibitors) and incubated at +4 °C for 30 min, followed by centrifugation (10,000x g for 10 min, +4 °C). 20 µl of the supernatant was kept aside as the lysate control. The remainder of the supernatant was incubated with GFP-Trap beads (ChromoTek; gtak-20), which bind to both GFP and to complemented Venus (V1+V2), for 1 h at 4 ºC. Finally, immunoprecipitated complexes were washed three times with wash-buffer (20 mM Tris-HCl pH 7.5, 150 mM NaCl, 1 % NP-40) and denatured for 5 min at 95ºC in reducing Laemmli buffer before SDS-PAGE analysis under denaturing conditions (4–20% Mini-PROTEAN TGX Gels). The proteins were then transferred to nitrocellulose membranes (Bio-Rad Laboratories) before blocking with blocking buffer (Thermo, StartingBlock (PBS) blocking, #37538) and PBS (1:1 ratio). The membranes were incubated with primary antibodies diluted in blocking buffer overnight at 4°C. Following this step, membranes were washed three times with TBST and incubated with fluorophore-conjugated secondary antibodies (LI-COR) diluted (1:10,000) in blocking buffer at room temperature for 1 hour. Membranes were scanned using an infrared imaging system (Odyssey; LI-COR Biosciences).

Antibody immunoprecipitation of endogenous proteins were performed on MDA-MB-231 cell lysates (one 10 cm dish per condition). Cells were washed with PBS and harvested in 200 µl of IP-lysis buffer (see above). SureBeads Protein G Magnetic beads (Bio-Rad Laboratories, #161-4023) were thoroughly resuspended in their solution, and 100 µl (1 mg at 10 mg/ml) were transferred to a 1.5 ml tube. The beads were then magnetized and the supernatant discarded, after which the beads were washed three times with PBS-T (0.1% Tween). 2 µg of antibody or isotype matching IgG control (Supplementary Table 2) was added to the beads and kept at room temperature under rotation for 30 min, after which the beads were magnetized, supernatant was discarded and beads were washed 3x with PBS-T. Cell lysate was then added to the beads and allowed to rotate for 1 h at room temperature. 25 µl of total lysate was set aside for total lysate control. Beads were then magnetized, supernatant discarded and beads were washed 3x with TBS-T, after which samples were centrifuged for several seconds at 600 x g. Beads were then magnetized and residual buffer was aspirated off, before addition of sample buffer, boiling (10 min at 95ºC) and separation using SDS-PAGE. Protein transfer and detection was performed as described above.

Protein purification

For producing recombinant GST-tagged proteins, (Rab21 16-225, Swip1, GGA3), pGEX-4T1-Rab21 16-225, pGEX-4T1-Swip1 or pGEX6P1-GGA3-BL21 Rosetta transformed cells

were grown and induced with 250 µM IPTG at OD 0.5-0.8 at 22°C in LB media overnight. Cells were then lysed and resuspended in 20 mM Tris, pH 7,5; 5 mM $MgCl_2$, 300 mM NaCl, 3 mM DTT. The desired GST-tagged protein was purified from this suspension with a gravity GST-column. In the case of GST-Rab21, elution of the protein was followed by thrombin-cleavage and gel filtration in 20 mM Tris, pH 7.5, 5 mM $MgCl_2$, 50 mM NaCl, 3 mM DTT buffer using a Superdex S75 16/60 column attached to a GST-column to bind cleaved GST. Fractions containing the monomeric proteins were pooled, concentrated via ultrafiltration (Amicon Ultra, 15 mL, 10,000 MWCO) and flash-frozen in liquid nitrogen for long-term storage at -80°C.

For producing His-fusion proteins (IRSp53, VASP and ARF1), E. coli BL21 Rosetta (DE3) cells picked from individual colonies were used to inoculate 200 mL of LB medium (containing ampicillin at 50 µg/mL) and were grown overnight at 37 °C. Between 10 and 100 mL of the overnight culture was diluted in 1 l of LB and was grown at 37 °C (240 rpm shaking) until it reached approximately OD = 0.4–0.6. Then, IPTG (1 mM) was added and after the induction cells were pelleted down at 4000 x g for 15 min at 4 °C and pellets were used immediately or conserved at −80 °C after washing in PBS. Bacterial pellets were resuspended in His-lysis buffer (50 mM Tris pH 8, 300 mM NaCl, 10 mM imidazole, 1mM β-mercaptoethanol, protease inhibitor cocktail (Roche, Basel, Switzerland), 10% glycerol); samples were sonicated 3 times for 30 s/each on ice and were pelleted down at 30,778 x g for 30 min at 4 °C using a JA 20 Beckman rotor or at 100,000 x g for 45 min at 4 °C using a 55.2 Ti Beckman rotor. A total of 600 µL of NiNTA beads (Qiagen), previously washed 3 times with His-lysis buffer, was added to the supernatant and samples were incubated 1–2 h at 4 °C while rocking. Beads were then washed 2 times in 20 mM imidazole, 600 mM NaCl, 50 mM Tris pH 8, 1 mM β-mercaptoethanol, 10% glycerol and one time in 40 mM imidazole, 300 mM NaCl, 50mM tris pH 8, 1 mM β-mercaptoethanol, 10% glycerol (5 min, 4 °C). Beads were packed in Poly-Prep® Chromatography Columns (BioRad) and eluted with 200 mM imidazole, 50 mM Tris pH 8, 200 mM NaCl, 1 mM β-mercaptoethanol, 10% glycerol (500 µl fractions). Fractions, evaluated by Bradford assay and SDS-PAGE, were pooled together and dialyzed. Samples were aliquoted, flash frozen and stored at -80 °C in 50 mM Tris pH 7.5, 200 mM NaCl, 1 mM DTT, 10% glycerol.

Nucleotide loading and GST pulldowns

To load Rab21 with either GppNHp or GDP, 200 µM of recombinant Rab21 or GST-Rab21 were incubated with 10 mM EDTA and a 25x excess of nucleotide (5 mM GppNHp or GDP)

in exchange buffer (20 mM Tris pH 7.5, 2.5 mM $MgCl_2$, 50 mM NaCl and 3 mM DTT) for 1 h at 25 °C. The EDTA-based exchange reaction was then stopped by the addition of 40 mM $MgCl_2$ and incubation for 15 min on ice. The buffer was then exchanged with measuring buffer (20 mM Tris, pH 7.5, 5 mM MgCl2, 50 mM NaCl and 3 mM DTT) to reach the desired protein concentration using 10 kDa ultrafiltration devices (Amicon). Equal amounts of nucleotide compared to the protein amount was added to ensure complete loading of Rab21 with the desired nucleotide.

GST pulldowns using purified GST fusion proteins and recombinant Rab21 bound to a non-hydrolysable form of GTP (GppNHp), GDP or no nucleotide (in the presence of EDTA) were performed as follows. 50 µg of GST-Swip1 or GST-Appl1 was incubated with 200 µg of recombinant Rab21 for 30 min before incubation with Glutathione Sepharose beads for an additional 30 min. The proteins bound to the beads were divided in two fractions and separated by SDS-PAGE electrophoresis, followed by either Coomassie staining or immunoblotting with anti-Rab21 antibody. Pulldowns were performed three times.

Overlay assay

Nitrocellulose membranes were incubated in TBST 0.1% Triton X- 100 buffer and let do dry. Equal or increasing amounts of recombinant-purified proteins were spotted on membranes and let dry. Membranes, previously blocked in TBST 0.1% Triton X-100 5% Milk, were then incubated with the recombinant protein of interest, resuspended in TBST 0.1% Triton X-100 5% Milk, 1–2 h at 4 °C. After extensive washing in TBST 0.1% Triton X-100, membranes were subjected to western blot analysis with the desired antibodies.

In vitro binding GST-Swip1/Arf1 T31N/Q71L

Cell lysates from HEL293T cells transfected with HA-tagged ARF1 T31N or ARF1Q71L (lysis buffer: 50 mM Tris HCl pH 7.4, 150 mM NaCl, 10 mM MgCl2, 1% Triton X-100, 1 mM DTT, protease inhibitor cocktail) were incubated with equal amounts (2 µM) of GST-Swip1 or GST as control for 1 h at 4 °C. Reactions were washed three times in lysis buffer. After washing, beads were resuspended in 1:1 volume of 2x SDS-PAGE Sample Buffer, boiled for 10 min at 95 °C, centrifuged for 1 min and then loaded onto polyacrylamide gels.

SIM microscopy and co-localization analysis

Cells growing on uncoated glass or collagen-1-coated dishes were fixed with 2% formaldehyde, permeabilized with 0.3 % Triton X-100, blocked with 10 % horse serum and incubated with antibodies against the indicated endogenous proteins. This was followed by incubation with fluorophore-labelled secondary antibodies (Alexa-568, Alexa-488 or Alexa-647 anti-mouse or anti-rabbit, Life Technologies). For visualization of Swip1-containing invaginations, cells expressing mScarlet-I-Swip1 were incubated at 4°C for 30 min before fixation. Cells were imaged with an OMX DeltaVision and spots co-localization analysis was performed in Z stacks of the cells using the plugin ComDet in ImageJ (https://imagej.net/Spots_colocalization_(ComDet)), which allowed for a better detection of the invaginations since it ignores inhomogeneous cytoplasmic background. Using this plugin, we pinpointed the mScarlet-I-Swip1 spots (pixel size above 5), and analyzed co-localization, based on proximity (pixel distance 4), with spots from the second channel stained for the protein of interest. Then, the ratio of co-localization with mScarlet-I-Swip1 was calculated as a percentage of co-localized spots per cell. At least 30 cells per condition were imaged and analyzed. Co-localization plots show mean ± 95 % CI. Statistical significance was calculated compared to the control condition. Representative rendered images of the invaginations (x-z plane) were visualized with IMARIS software (Oxford Instruments, version 8.1.2).

Proximity Ligation Assay (PLA)

MDA-MB-231 cells growing on coverslips were fixed, washed twice with PBS and permeabilized with 0.3% Triton-X-100 in PBS for 15 min at room temperature. Cells were stained using anti-Swip1 (1:100) and anti-Rab21 (1:50) primary antibodies diluted in 5% horse serum for 1 h at room temperature. Proximity ligation was performed according to the manufacturer's instructions (Duolink in situ PLA, Sigma-Aldrich). Interaction between Swip1 and Rab21 in cells was detected using confocal microscopy (Leica TCS SP5, 63x/1.4 Apo oil objective) and the number of PLA spots per 1000 μm^3 was quantified using IMARIS software. For the PLA between active β1-integrin (12G10) and IRSp53, MDA-MB-231 cells growing on glass-bottom dishes (and for Fig. 4i, expressing GFP or GFP-Swip1) were incubated at 4 °C for 30 min before fixation, after which they were washed and permeabilized as indicated above. Cells were stained using 12G10 (1:100) and anti-IRSp53 (1:300) primary antibodies diluted in 5% horse serum for 1 h at room temperature. PLA was performed as indicated above and imaged using a 3i (Intelligent Imaging Innovations, 3i Inc) Marianas Spinning disk confocal microscope with a Yokogawa CSU□W1 scanner and a back

illuminated 10 MHz EMCDD camera (Photometrics Evolve) with a 63x/1.4 oil objective, controlled by the Slidebook (version 6) software.

BiFC and TIRF microscopy

MDA-MB-231 cells growing in glass-bottom dishes were co-transfected with split Venus constructs (pDEST-V1-Rab21 and pDEST-Swip1-V2) and imaged 30 h after transfection. Imaging was performed using a DeltaVision OMX v4 (GE Healthcare Life Sciences) fitted with an Olympus APO N 60x Oil TIRF objective lens, 1.49 NA used in TIRF illumination mode. Emitted light was collected on a front illuminated pco.edge sCMOS (pixel size 6.5 mm, readout speed 95 MHz; PCO AG) controlled by SoftWorx. The TIRF angle for all channels was maintained at 83.5º. Images were taken every 500 ms for 2 min, at 37 °C in presence of 5 % CO_2. Imaging of the above-mentioned BiFC constructs together with different endocytic vesicle markers was performed with a 3i (Intelligent Imaging Innovations, 3i Inc) Marianas Spinning disk confocal microscope with a Yokogawa CSU□W1 scanner and a back illuminated 10 MHz EMCDD camera (Photometrics Evolve) using 63x/1.4 oil objective. Cells were fixed with 2% formaldehyde, permeabilized with 0.3 % Triton X-100, blocked with 10 % horse serum and incubated with antibodies against the indicated endogenous proteins. This was followed by incubation with fluorophore-labelled secondary antibodies (Alexa-568, Alexa-488 or Alexa-647 anti-mouse, anti-rabbit or anti-goat, Life Technologies).

DNA Paint

For two-color single molecule localization microscopy (SMLM) (Extended Data Fig. 4a), we used DNA-PAINT [24]. Cells over-expressing Swip1-GFP and ARF1-HA were fixed and labeled using primary antibodies against GFP (Abcam ab1218) and HA-tag (Cell Signaling 3724), respectively. Cells were then stained with appropriate secondary antibodies coupled to PAINT DNA handles (Ultivue). Imaging was performed using a DeltaVision OMX v4 (GE Healthcare Life Sciences) fitted with an Olympus APO N 60x Oil TIRF objective lens, 1.49 NA used in TIRF illumination mode. Emitted light was collected on a front illuminated pco.edge sCMOS (pixel size 6.5 mm, readout speed 95 MHz; PCO AG) controlled by SoftWorx. First, a TIRF image of Swip1-GFP was acquired, followed by the DNA-paint acquisitions.

DNA paint imaging was done sequentially first for Swip1-GFP (10 000 frames, 50 ms) and for ARF1 (10 000 frames, 100 ms) in PAINT buffer (10 mM Tris-HCl, 100 mM NaCl, 0.05

% Tween-20, pH 7.5) supplemented with 0.5 nM of the corresponding PAINT imager strands coupled to AlexaFluor 647 (Swip1-GFP) or to AlexaFluor 568 (ARF1). For both conditions, full laser power was used and the beam concentrator enabled. No cross-talk between the channels was observed. The ThunderSTORM [55] ImageJ plugin [56], with the Phasor-based localization 2D method [57], was used for the localization of single fluorophores. After filtering out localizations to reject too low photon counts, translational shifts were corrected by autocorrelation. Image reconstructions were performed using the ThunderSTORM ImageJ plugin.

Uptake/endocytosis assays

MDA-MB-231, MDA-MB-468 and BT-20 cells were grown on uncoated plastic dishes or glass coverslips unless stated otherwise. For integrin endocytosis assays, surface integrins were labelled with an antibody that recognizes the active conformation of β1-integrins (12G10) at 4 °C followed by incubation at 37 °C for 15 min unless stated otherwise. The antibody still left on the surface was washed away with acid (0.2 M Acetic acid, 0.5 M NaCl pH 2.5). The cells were subsequently fixed with 2% formaldehyde, permeabilized with 0.05% saponin and incubated with a fluorescent secondary antibody to visualize and quantify the amount of internalized integrins. Several fields were randomly imaged with identical microscope settings using a 3i (Intelligent Imaging Innovations, 3i Inc) Marianas Spinning disk confocal microscope with a Yokogawa CSU□W1 scanner and a back illuminated 10 MHz EMCDD camera (Photometrics Evolve) using 63x/1.4 oil objective. Quantification of endocytosed integrins was performed on 3D-projections of the cells using IMARIS software with the spots detection function. The intensity sum of all the vesicles per cell was divided by the volume of that cell. All the intensity values were then normalized to the average of all the cells in the control condition (siCTRL). A similar procedure was followed for the uptake of MHCI (SAB4700637 Sigma) and 9EG7 (active β1-integrin).

For AlexaFluor 568-labelled transferrin (Transferrin-AF568, Thermo Fisher T23365) and 10 kDa dextran uptake experiments, MDA-MB-231 cells were treated with 1 mg/mL of transferrin, 10 kDa dextran-TMR (D1816, Invitrogen) or 10 kDa amino dextran (Molecular Probes) conjugated to FITC during the 15 min incubation at 37°C. In the case of the double uptake experiments, cells were previously labelled with 12G10-AF488 antibody (Abcam, ab202641) at 4 °C as described above. After the internalization step at at 37°C, the remaining fluorescently labelled molecules at the cell surface were removed with an acid wash,

followed by fixation, labelling of plasma membrane with WGA lectin and imaging as described above.

Surface biotinylation-based integrin trafficking assays were performed based on previously published methods [58,59] with some modifications. ELISA plates were prepared by coating Nunc MaxiSorb 96-well plates (#44-2404-21, Thermo Fischer) with 50 µl/well 5 µg/ml anti-integrin antibody in TBS o/n at +4 °C (see table for antibody details). Wells were blocked with 5% BSA in TBS for 2 h +37 °C. MDA-MB-231, silenced three days prior to the experiment as described above, were grown in 10% FCS-containing medium on 6 cm dishes to 80% confluence. The cells were placed on ice and washed once with cold PBS. Cell surface proteins were labelled with 0.13 mg/mL of EZ-link cleavable sulfo-NHS-SS-biotin (#21331; Thermo Scientific) in serum-free DMEM for 30 min at +4 °C. Unbound biotin was washed away with cold medium, and cells were incubated 15 min on ice in cold serum free DMEM with or without 100 µM primaquine (#160393 Sigma; PQ). Pre-warmed serum-free DMEM (with or without PQ) was added to cells. The biotin-labelled surface proteins were allowed to internalize at +37 °C for the indicated time points, after which the cells were placed quickly back on ice and rinsed with cold DMEM and with cold cell surface reduction buffer (50 mm Tris–HCl, pH 8.6, 100 mm NaCl). The remaining biotin at the cell surface after internalization was removed with 30 mg/ml MesNa (63705; sodium 2-mercaptoethanesulfonate: Fluka) in MesNa buffer for 20 min at 4 °C, followed by quenching with 100 mM iodoacetamide (Sigma) for 15 min on ice. To detect the total amount of surface biotinylation, one of the cell dishes was left on ice after biotin labelling followed by treatment without reducing MesNa. For the 0 min internalization, cells were maintained on ice in serum-free DMEM until cell surface reduction with MesNA. The cells were lysed by scraping in lysis buffer (1.5% octylglucoside, 1% NP-40, 0.5% BSA, 1 mM EDTA protease and phosphatase inhibitors) and incubation at +4 °C for 20 min. Cell extracts were cleared by centrifugation (16 000 × *g*, 10 min, 4 °C). To determine the amount of internalized, biotinylated integrins, 50 µl of cell lysates were incubated in duplicate wells o/n +4 °C, washed extensively with TBS-T, incubated 2 h +4 °C with 1:1000 HRP-coupled streptavidin (#21130 Fisher) washed and detected with antibody for ELISA detection.

For the FACS-based EGFR endocytosis assay, adherent cells were labeled with 1:500 extracellular domain-binding EGFR antibody (#05-101, UpState) on ice for 30 min. Unbound antibody was washed away, and the cells were chased in warm medium in the presence or absence of 10 ng/ml EGF. Cells were washed with cold PBS and carefully collected by scraping. Cells were fixed for 10 min at 4 °C with 4% PFA, washed, and suspended in PBS

followed anti-mouse AlexaFluor 647 secondary antibody (dilution 1:300 in PBS; from Invitrogen), washed with PBS and analysed with LSRFortessa (BD Biosciences). Data analysis was performed with Flowing software version 2 (Cell Imaging Core of the Turku Bioscience Centre). The geometric mean of the fluorescence intensity from cells labelled with secondary antibody alone was used as background and subtracted from the stained samples. For normalization, the background-corrected values were divided by the sum of all signals within one independent experiment. Representative raw flow cytometry data can be found in Supplementary Figure 1.

Hypotonic-isotonic shocks

MDA-MB-231 cells were transfected with either siCTRL, siRNA #1 or siRNA #2 against Swip1 and used 96 hours after silencing. Cells were kept in either isotonic (100% incomplete DMEM) or hypotonic media (50% incomplete DMEM, 50% sterile double distilled water) for 1 min, followed by pulse of various cargos in isotonic media for 1 min. Pulse contained the following cargos: anti-β1-integrin antibody (12G10 conjugated to AlexaFluor 488, 2 ug/ml), 1 mg/ml 10 kDa dextran conjugated to tetra methyl rhodamine and 10 ug/ml transferrin conjugated to AlexaFluor 647. After the pulse, surface-bound cargoes were stripped with 0.2 M Acetic acid, 0.5 M NaCl pH 2.5 for 3 min on ice and then fixed with 2% PFA. Then, cells were imaged with confocal microscopy as described above and the cell mean intensity of each cargo was quantified using manual segmentation with ImageJ.

Electron microscopy and Apex labelling

Apex labeling of GFP-Swip1 for electron microscopy was performed as previously described [35]. Briefly, MEFs were transfected with GFP-Swip1 and GBP-Apex (Addgene plasmid #67651) constructs using a Neon transfection system (as per manufacturer's instructions) and plated into 35 mm tissue culture dishes. 24 h post-transfection, cells were incubated on ice for 30 min, then fixed in 2.5 % glutaraldehyde, washed 3x in cacodylate buffer and once in 1 mg/ml 3,3′-diaminobenzidine (DAB; Sigma-Aldrich) solution in cacodylate for 5 min. Cells were then subjected to the DAB reaction in the presence of H_2O_2 for 30 min and, stained with 1 % osmium tetroxide for 2 min. The cells were processed in situ with serial dehydration in increasing percentages of ethanol, then serial infiltration with LX112 resin in a Pelco Biowave microwave before polymerizing overnight at 60 °C. Ultra-thin (60 nm) sections

were cut on a Leica UC6 microtome parallel to the culture dish and micrographs acquired using a Jeol 1011 transmission electron microscope.

Vesicle tracking

For Rab21 vesicle tracking, MDA-MB-231 cells stably expressing GFP-Rab21 were transfected with one of two different siRNA sequences to deplete the levels of Swip1. In the rescue experiment (Fig. 6i), control- and Swip1-silenced cells were transfected with GFP-Rab21 and either mScarlet-I-Swip1 or mScarlet-I-ΔEF1-Swip1. The movement of the Rab21 vesicles was followed for 2 min using TIRF microscopy (Visitron SD-TIRF Nikon Eclipse TiE with a 60x Olympus TIRF oil objective, NA: 1.49 or DeltaVision OMX v4 as described in the BiFC and TIRF microscopy section). GFP-Rab21 vesicles were imaged for 2 minutes in each cell, every 500 milliseconds. The TIRF angle was kept constant at 85.5°. The vesicles were detected and tracked using the spots tracking function in IMARIS software. The parameters used in the algorithm were an estimated diameter of spots/vesicles of 0.5 μm, background subtraction and Brownian motion for modelling the vesicle movement, with a maximum distance of 20 μm for displacement length and a maximum gap size of 3 μm between spots. We used the mean speed of all vesicle tracks in one cell to then calculate the average speed of vesicles per cell. At least 10 cells per condition were analyzed and data from 3 independent experiments was quantified.

Focal adhesion analysis

Cells were plated on dishes coated with the indicated extracellular matrix component (collagen I, laminin-1 or fibronectin), fixed and immunostained with an antibody that recognizes the focal adhesion component vinculin, present in mature adhesions. At least 6 cells per condition per experiment were imaged and analyzed (18 cells per condition in total from 3 independent experiments). Vinculin-positive focal adhesions were detected from an image mask created using the ImageJ software following background subtraction and setting of median Gaussian filter (3.0). The number of focal adhesions (detected particles) and the total cell area occupied by focal adhesions per cell was quantified from the image mask.

Adhesion dynamics

For adhesion dynamics studies, MDA-MB-231 cells transiently expressing GFP-paxillin were transfected with one of two different siRNA sequences to deplete the levels of Swip1. GFP-

paxillin was imaged for 120 min at the TIRF plane with a Deltavision OMX using a 63x objective. Cells were imaged every 1 min, at 37 °C in presence of 5 % CO_2, using multiposition capabilities. Focal adhesion dynamics were then analyzed using the Focal Adhesion Analysis Server[60]. Only focal adhesions with a lifetime minimum of 10 frames were analyzed, and the focal adhesions that were assembled and disassembled during the course of imaging were used for measuring focal adhesion kinetics.

Focal adhesion proximity analysis

MDA-MB-231 cells expressing V1-Rab21, V2-Swip1 and mKate2-paxillin were imaged live using a TIRF microscope. Post-acquisition, images were denoised using Noise2Void [61] trained using the ZeroCostDL4Mic platform (v 1.11.1; [62]).

To denoise the Swip1-Rab21 movies, individual Noise2Void models were generated for each movie using 300 epochs, 12288 image patches, a batch size of 128, and a starting learning rate of 0.0004. To denoise the mKate2-paxillin images, a single Noise2Void model was generated using 300 epochs, 56064 image patches, a batch size of 128, and a starting learning rate of 0.0004. Post-denoising, individual focal adhesions were automatically segmented using the focal adhesion server [60] while individual Swip1-Rab21 puncta were semi-automatically segmented using the Trainable Weka Segmentation tool implemented in Fiji [63]. The nearest distance between Swip1-Rab21 puncta and paxillin-positive focal adhesion was measured using the Distance Analysis (DiAna) Fiji plugin [64]. Images containing randomly distributed puncta within the cells (to assess their distance to focal adhesion) were generated using a custom Fiji macro (available as a Zenodo package as described below) [65].

Random cell migration

Cells were seeded in 24-well plates (Greiner Bio-One) one day before imaging. The media was supplemented with 500 nM SiR-DNA (Cytoskeleton Inc) 2 h before imaging. Cells were then imaged live (37 °C, 5% CO_2) using a Nikon Eclipse Ti2-E microscope (Nikon) equipped with a sCMOS Orca Flash4.0 camera (Hamamatsu) and controlled by the NIS-Elements software (Nikon, v 5.11.01). Cells were imaged using a 20x Nikon CFI Plan Apo Lambda objective (NA 0.75) one frame every 10 minutes for 16 h. Cell nuclei were automatically segmented over time using the deep learning algorithm StarDist implemented in the ZeroCostDL4Mic platform and tracked using TrackMate[62,66–68]. In particular, a custom

StarDist model was generated using the ZeroCostDL4Mic platform [62]. This custom StarDist model was trained for 300 epochs using 46 manually annotated paired images (image dimensions: (1024, 1024)) with a batch size of 2, an augmentation factor of 4 and a mae loss function. The StarDist "Versatile fluorescent nuclei" model was used as a training starting point. Key python packages used include TensorFlow (v 0.1.12), Keras (v 2.3.1), CSBdeep (v 0.6.1), NumPy (v 1.19.5), Cuda (v 11.0.221). The training was accelerated using a Tesla P100GPU. Tracking was performed using a TrackMate script available here (https://github.com/HenriquesLab/ZeroCostDL4Mic/tree/master/Tools/Automated_tracking) and using the following settings: Linking max distance = 150 pixels, gap closing distance = 20 pixels, Max frame gap =1. Cell tracks were combined in R using the script available here (https://github.com/HenriquesLab/ZeroCostDL4Mic/tree/master/Tools/Automated_tracking) and further analysed using the Motility Lab website (http://www.motilitylab.net/). The associated data used for analysis is available as Zenodo packages: the training dataset and the StarDist model used for the automated tracking [69] and the archive source code used in the analyses [65]. Plots to visualize cell track speed and mean displacement were made using plotsofdata (1.05) [70].

Scratch-wound migration assay

After siRNA transfection, MDA-MB-231 cells were seeded into ibidi 2-well culture inserts placed in ibidi µ-dishes and allowed to become confluent. Prior to imaging, the culture inserts were carefully removed with forceps and the cells were washed twice with PBS. Next, warm medium was added to the cells, after which live imaging was started immediately (37 °C, 5 % CO_2). Cells were imaged using a Nikon Eclipse Ti2-E microscope with a 10x objective for 24 h with a 20 minute imaging interval. Data was quantified using Fiji (ImageJ) by measuring the area of the closing gap between the cells at 0, 6, 8, 12, 16, and 18 h.

Invasion assay

200 µl of PureCol EZ gel (#5074; Advanced Biomatrix) was allowed to polymerize in 8 µm inserts (#662638; Greiner Bio-One) for 1 h at 37 °C. Inserts were then inverted and 100 µl of cell suspension (50000 cells) were seeded onto the outer face of the insert. Cells were allowed to adhere at 37 °C for 3 h. Inserts were then dipped sequentially into PBS and placed in serum-free medium. Medium supplemented with 10 % of FCS and 20 ng/ml of EGF was placed on top of the matrix and cells were allowed to invade the matrix for 72 h. Cells were

then fixed using 4 % PFA for 2 h, permeabilized in 0.3 % Triton-X 100 for 1 h at room temperature, and stained overnight at 4 °C using Alexa Fluor 488 phalloidin. Invading cells were imaged using a confocal microscope (LSM880; Zeiss). Invasion was quantified using the area calculator plugin in ImageJ, measuring the fluorescence intensity of cells invading 60 µm or more and expressing this as a percentage of the fluorescence intensity of all cells within the matrix.

Breast cancer tissue microarrays

The study was approved by the Hospital District of Southwest Finland and Turku University Hospital (decision T012/015/19) and the use of tissue samples was approved by the Scientific Steering Group of Auria Biobank (decision AB19-4522). The study population consisted of 243 patients with breast cancer diagnosed and treated in Turku University Hospital in 1998-2013. Informed consent was obtained from all the participants. All patients were treated with surgical resection or mastectomy and the archived formalin-fixed, paraffin-embedded tumor samples were used to form tissue microarrays (TMAs) that were prepared similarly as previously described [71]. Briefly, the TMAs were prepared by punching a representative site of paraffin block of each tumor with either a 1 mm or a 1.5 mm diameter cylinder and using an automated tissue arrayer (TMA Grand Master, 3DHISTECH Ltd., Budapest, Hungary).

The cohort consisted of 149 patients with triple negative and 89 patients with HER2-positive breast cancer diagnosed using the WHO classification criteria of tumors of the breast at the time of sampling. In addition, 4 patients with hormone receptor positive and 1 with non-neoplastic breast cancer were included in the TMAs. The cores were available from 225 tumor centers, 121 tumor borders, 26 lymph node metastases and 127 tumor areas with inflammatory infiltrate.

All relevant medical records of the patients were reviewed and information on tumor size, histological grade, hormone receptor status, Her2-oncogene, proliferation marker Ki-67 and axillary lymph node status were gathered. The follow-up time was until 31st March 2020 and the range of follow-up varied from 1 month to 22 years 3 months (mean 10 years 2 months).

Immunohistochemistry

Immunohistochemistry was performed on TMAs comprising one or two tissue cores from each tumor site of each patient. The tissue samples were cut into 4 µm sections,

deparaffinized and rehydrated with standard procedures. Heat-mediated antigen retrieval was done for all samples in citrate buffer (pH 6) in a pressure cooker (Decloaking chamber, Biocare Medical NxGen) for 20 min. Sections were stained in a semi-automatic Labvision autostainer (Thermo-Fisher Scientific), where they were washed with washing buffer (0.05 M Tris-HCl pH 7.6, 0.05 % Tween 20) and the endogenous enzymes were blocked with 3 % H_2O_2 Tris-HCl for 10 min. This was followed by a blocking step using Normal Antibody Diluent (NABD; Immunologic, BD09-125), incubation with the primary antibody (anti-Swip1, Atlas Antibodies, diluted 1:200) for 1 h, followed by washes and incubation with the secondary antibody (Goat anti-rabbit HRP, Immunologic DPVB110HRP) for 30 min. Samples were then washed and incubated with the DAB solution (Bright DAB, Immunologic BS04-110) for 10 min. After counterstain with Mayer's HTX, slides were dehydrated, cleared in xylene and mounted with Pertex. Antibody specificity was validated on agarose-embedded cell pellets post siRNA transfection (siCTRL, Swip1 siRNA #1 and Swip1 siRNA #2; Extended Data Fig. 10b).

For each tumor sample, the percentage of cells with immunopositive signal (0-100%) in cytoplasm and in plasma membrane were scored. Samples with more than 80% of cells exhibiting positive staining were considered as having high Swip1, those with less than 30 % of cells as low Swip1 and samples in between were considered to have medium Swip1 levels.

Statistical analysis for clinical samples

The statistical analysis was performed with SPSS Statistics 26 (IBM Corp., NY, USA). Two-tailed p values below 0.05 were considered statistically significant. The clinical parameters (age, tumor size and ki67) across Swip1 categories (<100 and 100, or <80 and ≥80) were evaluated with independent-samples double-sided Mann-Whitney U tests. The categorical parameters (grade and lymph node metastasis status) were compared with Chi Squared tests or Fisher's exact tests across Swip1 categories. Related-samples Wilcoxon signed rank test was used for paired comparisons of tumor centers and other core types. Patients with missing data were censored from the paired comparisons.

Overall survival was compared between low and high percentage of immunopositive cells in the tumor center samples of Her2+ and TNBC patients using Kaplan-Meier plots and log-rank tests: the samples were divided into the following groups: <100% or 100% in the case of the cytoplasmic signal and <80% or ≥80% in the case of membranal Swip1 signal.

The Cox proportional hazards regression analysis was used to assess the hazard ratio of tumor centers with high vs. lower Swip1 immunopositivity. In the case of non-proportional hazards, the weighted estimation of Cox regression was used [72]. The adjusted Cox analysis was performed relative to the clinical prognostic features. The analysis was performed with R Software for Statistical Computing (version 3.6.2, www.r-project.org) and survival (version 3.1.8) and coxphw (version 4.0.2) packages. Survival differences were quantified as hazard ratios (HRs) with 95% confidence intervals (CI).

Statistics & Reproducibility

Experiments were repeated at least 3 times to ensure reproducibility. All attempts at replication were successful. Key experiments were reproduced by different coauthors in different laboratories around the world. No statistical method was used to predetermine sample size. The standard in the field, a minimum of three, was selected for most experiments. No data were excluded from the analyses. For immunofluorescence analysis, randomization was ensured by taking representative pictures of different fields (or individual cells) from the same sample at different locations within the sample. Scoring of immunosignal in tissue samples was performed blindly by the pathologist. After scoring, the Biobank scientist correlated the scored values with the patient identifier and corresponding clinical information.

The two-sided Signifance B test was used to identify relevant interactors of Rab21 from the proteomics dataset. No multiple hypothesis correction method was applied, due to the small number of selected proteins for the statistical analysis. Abundance bins were defined by including 1000 proteins in a subsequent order.

The GraphPad Prism software and two-tailed Student's t test (paired or unpaired, as appropriate) was used for statistical analysis of *in vitro* experiments. When data were not normally distributed, a two-sided Mann−Whitney test was used. For the ELISA-based trafficking assay and the scratch-wound migration assay, statistical significance was determined using multiple comparison t-tests for paired data, with the post hoc Holm-Sidak method, with alpha=5.000%. Each row was analyzed individually, without assuming a consistent SD.

The number of cells analyzed for experiments in Figures 4, 5 and 7 is defined as follows:

Figure 4. Number of cells analyzed over 3 independent experiments: (a) siCTRL, 86, 101, 110 and 78; Swip1 siRNA#1, 104, 98, 102 and 106; from left to right. (b) siCTRL+GFP, 153;

siCTRL+GFP-Swip1, 186; siSwip1+GFP, 136 and siSwip1+GFP-Swip1, 196. (c) siCTRL, 107, Swip1 siRNA#1, 116, siRab21, 122 (d) α2 integrin-WT, 70 and mutant α2 integrin-AA, 76. (e) siCTRL, 50 and siRab21, 56 (h) siCTRL+GFP, 157; siCTRL+GFP-Swip1, 289; siIRSp53+GFP, 108 and siIRSp53+GFP-Swip1, 136. (i) GFP, 106 and GFP-Swip1, 111.

Figure 5. Number of cells analyzed over 3 independent experiments: (a) Dextran-FITC, 18 and 21 and β1-integrin-A488, 22 and 21. (b) siCTRL, 160; Swip1 siRNA#1, 157; Swip1 siRNA#2, 160; siCTRL, 121; IRSp53 siRNA#1, 177 and IRSp53 siRNA#2, 121. (c) siCTRL, 152; Swip1 siRNA#1, 125 and IRSp53 siRNA#1, 92. (d) For BT-20 12G10 and MHCI uptake, respectively, siCTRL, 79 & 91; Swip1 siRNA#1, 76 & 91; Swip1 siRNA#2, 66 & 75. For MDA-MB-468 12G10 and MHCI uptake, respectively, siCTRL, 134 & 155; Swip1 siRNA#1, 98 & 156; Swip1 siRNA#2, 98 & 135 (e) For dextran uptake, without (-) or with (+) hypotonic shock, respectively: siCTRL, 227 & 220; Swip1 siRNA#1, 208 & 186; Swip1 siRNA#2, 208 & 187. For β1-integrin uptake, without (-) or with (+) hypotonic shock, respectively: siCTRL, 195 & 191; Swip1 siRNA#1, 208 & 181; Swip1 siRNA#2, 181 & 139. (f) siCTRL, 50 and siRab21, 56.

Figure 7. Number of cells analyzed over 3 independent experiments: (a) collagen I, 65, 76 & 67; fibronectin, 65, 75 & 62; laminin-1, 62, 66 & 73 for siCTRL, siSwip1 siRNA #1 and siRNA #2, respectively. (b) 18 cells per condition; FAs analyzed: siCTRL, 861 & 764; and siSwip1, 1014 & 1024 for assembly and disassembly, respectively. (c) 20 cells per condition, 697 BiFC puncta and 1364 randomly distributed puncta.

Data Availability:

The data that support the findings of this study are available within the paper [and its supplementary information files] or from the corresponding author upon reasonable request. The proteomics data have been deposited to the ProteomeXchange Consortium via the PRIDE partner repository with the dataset identifier PXD016478.

Code Availability

Custom code written to perform the migration analyses has been deposited to Zenodo (https://zenodo.org/record/4812018#.YK5JdHUzaV4). Deep Learning model used to analyze the cell migration data has also been deposited to Zenodo (https://zenodo.org/record/4811213#.YK5FGnUzaV4).

Methods References

51. Paul, F. E., Hosp, F. & Selbach, M. Analyzing protein-protein interactions by quantitative mass spectrometry. *Methods San Diego Calif* **54**, 387–395 (2011).

52. Cox, J. & Mann, M. MaxQuant enables high peptide identification rates, individualized p.p.b.-range mass accuracies and proteome-wide protein quantification. *Nat. Biotechnol.* **26**, 1367–1372 (2008).

53. Borchers, H. W. pracma: Practical Numerical Math Functions. (2019).

54. Perez-Riverol, Y. *et al.* The PRIDE database and related tools and resources in 2019: improving support for quantification data. *Nucleic Acids Res.* **47**, D442–D450 (2019).

55. Ovesný, M., Křížek, P., Borkovec, J., Svindrych, Z. & Hagen, G. M. ThunderSTORM: a comprehensive ImageJ plug-in for PALM and STORM data analysis and super-resolution imaging. *Bioinforma. Oxf. Engl.* **30**, 2389–2390 (2014).

56. Schindelin, J. *et al.* Fiji: an open-source platform for biological-image analysis. *Nat. Methods* **9**, 676–682 (2012).

57. Martens, K. J. A., Bader, A. N., Baas, S., Rieger, B. & Hohlbein, J. Phasor based single-molecule localization microscopy in 3D (pSMLM-3D): An algorithm for MHz localization rates using standard CPUs. *J. Chem. Phys.* **148**, 123311 (2018).

58. Farage, E. & Caswell, P. T. Quantitative Analysis of Integrin Trafficking. *Methods Mol. Biol. Clifton NJ* **2217**, 251–263 (2021).

59. Arjonen, A., Alanko, J., Veltel, S. & Ivaska, J. Distinct recycling of active and inactive β1 integrins. *Traffic Cph. Den.* **13**, 610–625 (2012).

60. Berginski, M. E. & Gomez, S. M. The Focal Adhesion Analysis Server: a web tool for analyzing focal adhesion dynamics. *F1000Research* **2**, 68 (2013).

61. Krull, A., Buchholz, T.-O. & Jug, F. Noise2Void - Learning Denoising from Single Noisy Images. *ArXiv181110980 Cs* (2019).

62. von Chamier, L. *et al.* Democratising deep learning for microscopy with ZeroCostDL4Mic. *Nat. Commun.* **12**, 2276 (2021).

63. Arganda-Carreras, I. *et al.* Trainable Weka Segmentation: a machine learning tool for microscopy pixel classification. *Bioinformatics* **33**, 2424–2426 (2017).

64. Gilles, J.-F., Dos Santos, M., Boudier, T., Bolte, S. & Heck, N. DiAna, an ImageJ tool for object-based 3D co-localization and distance analysis. *Methods San Diego Calif* **115**, 55–64 (2017).

65. Jacquemet, G. *Archived source code for Cargo-specific recruitment in clathrin and dynamin-independent endocytosis*. (Zenodo, 2021). doi:10.5281/zenodo.4812018.

66. Fazeli, E. *et al.* Automated cell tracking using StarDist and TrackMate. *F1000Research* **9**, 1279 (2020).

67. Tinevez, J.-Y. *et al.* TrackMate: An open and extensible platform for single-particle tracking. *Methods San Diego Calif* **115**, 80–90 (2017).

68. Schmidt, U., Weigert, M., Broaddus, C. & Myers, G. Cell Detection with Star-Convex Polygons. in *Medical Image Computing and Computer Assisted Intervention – MICCAI 2018* (eds. Frangi, A. F., Schnabel, J. A., Davatzikos, C., Alberola-López, C. & Fichtinger, G.) 265–273 (Springer International Publishing, 2018). doi:10.1007/978-3-030-00934-2_30.

69. Al-Akhrass, H., Ivaska, J. & Jacquemet, G. Stardist model and training dataset for automated tracking of MDA-MB-231 and BT20 cells. (2021) doi:10.5281/zenodo.4811213.

70. Postma, M. & Goedhart, J. PlotsOfData—A web app for visualizing data together with their summaries. *PLOS Biol.* **17**, e3000202 (2019).

71. Heuser, V. D. *et al.* Formin Proteins FHOD1 and INF2 in Triple-Negative Breast Cancer: Association With Basal Markers and Functional Activities. *Breast Cancer Basic Clin. Res.* **12**, 1178223418792247 (2018).

72. Dunkler, D., Ploner, M., Schemper, M. & Heinze, G. Weighted Cox Regression Using the R Package coxphw. *J. Stat. Softw.* **84**, 1–26 (2018).

1333

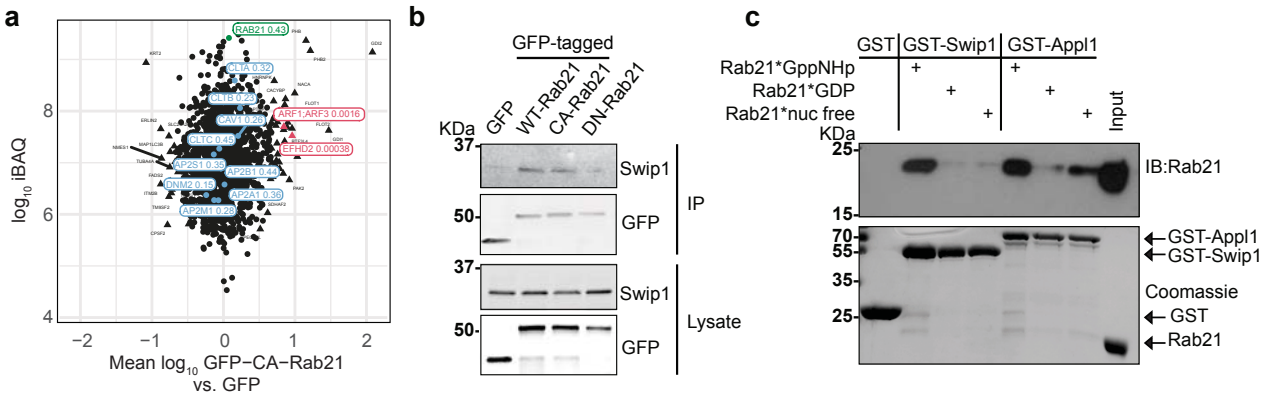
a
RAB21 0.43
CLTA 0.32
CLTB 0.23
CAV1 0.24
CLTC 0.45
AP2S1 0.24
AP2B1 0.44
DNM2 0.15
AP2A1 0.36
AP2M1 0.28
ARF1;ARF3 0.0016
EFHD2 0.00038
log10 iBAQ
Mean log10 GFP−CA−Rab21 vs. GFP
b
GFP-tagged
KDa
GFP
WT-Rab21
CA-Rab21
DN-Rab21
37
50
Swip1
GFP
IP
Lysate
c
GST
GST-Swip1
GST-Appl1
Rab21*GppNHp
Rab21*GDP
Rab21*nuc free
Input
KDa
25
15
70
55
35
IB:Rab21
GST-Appl1
GST-Swip1
Coomassie
GST
Rab21

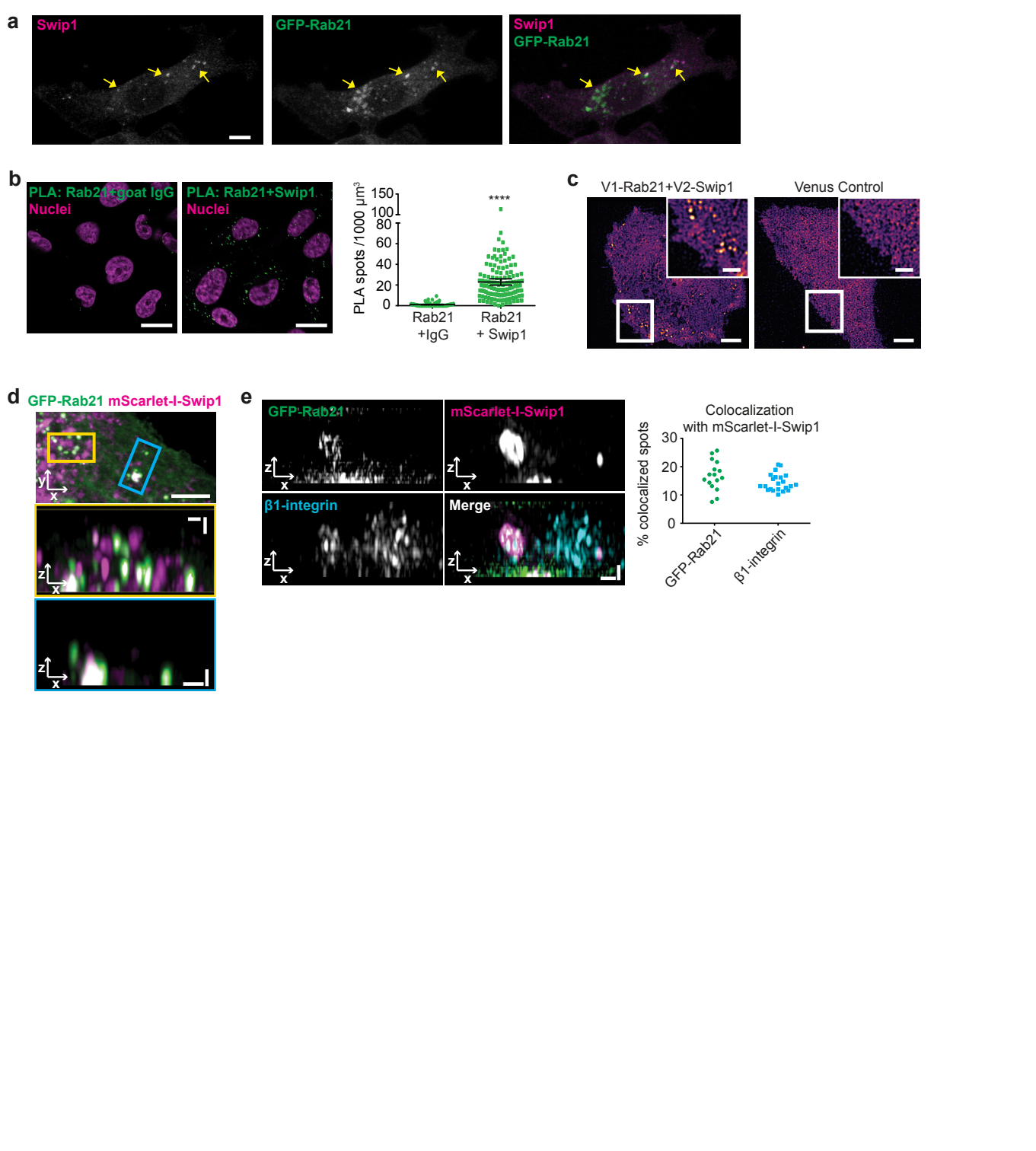
a
Swip1
GFP-Rab21
Swip1
GFP-Rab21
b
PLA: Rab21+goat IgG
Nuclei
PLA: Rab21+Swip1
Nuclei
PLA spots /1000 µm3
150
100
80
60
40
20
0
****
Rab21
+IgG
Rab21
+ Swip1
c
V1-Rab21+V2-Swip1
Venus Control
d
GFP-Rab21 mScarlet-I-Swip1
y
x
z
x
z
x
e
GFP-Rab21
mScarlet-I-Swip1
β1-integrin
Merge
Colocalization
with mScarlet-I-Swip1
% colocalized spots
30
20
10
0
GFP-Rab21
β1-integrin

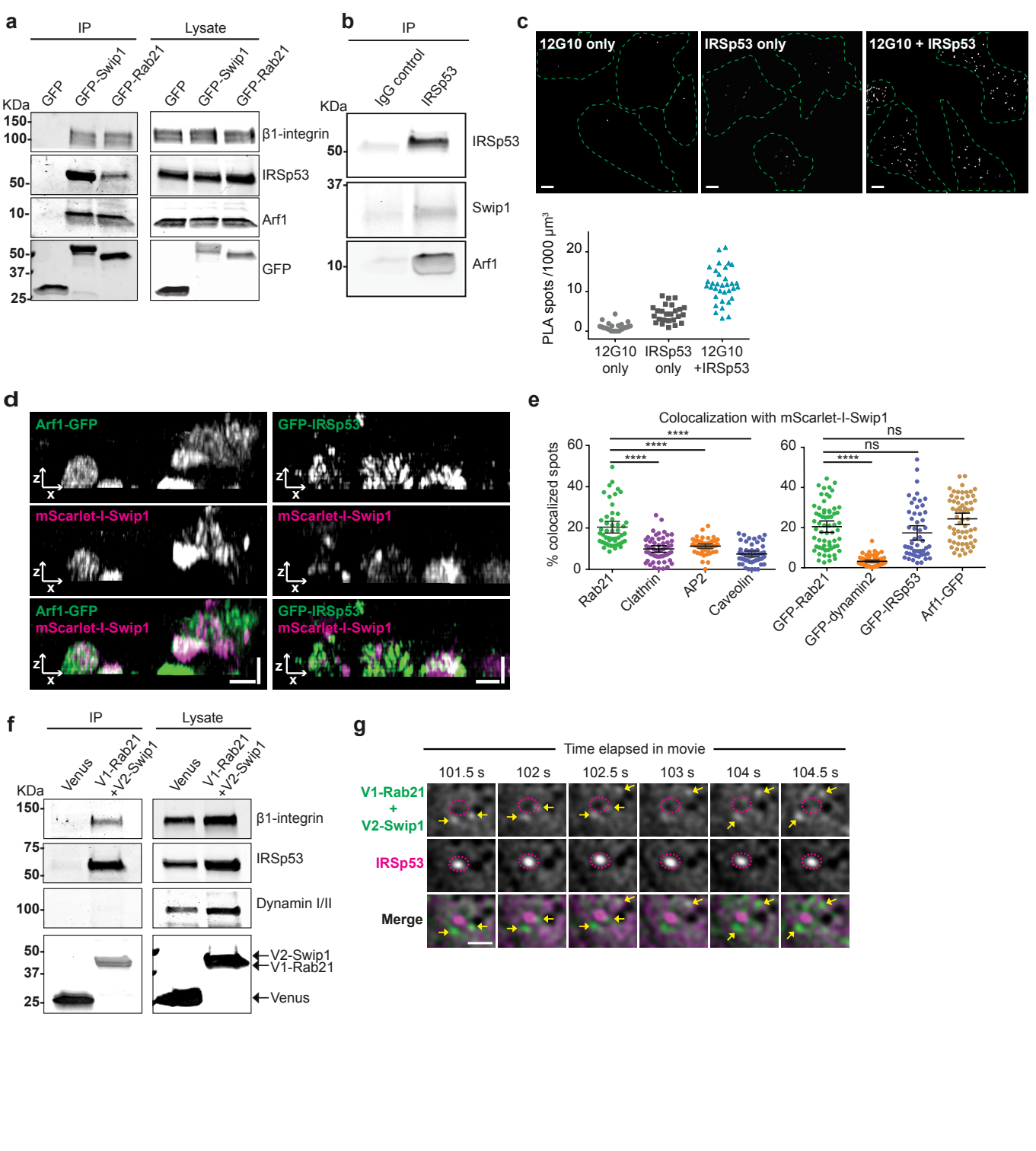
a
IP
Lysate
GFP
GFP-Swip1
GFP-Rab21
KDa
150
100
50
10
50
37
25
β1-integrin
IRSp53
Arf1
GFP
b
IP
IgG control
IRSp53
KDa
50
37
10
IRSp53
Swip1
Arf1
c
12G10 only
IRSp53 only
12G10 + IRSp53
PLA spots /1000 μm3
20
10
0
12G10 only
IRSp53 only
12G10 +IRSp53
d
Arf1-GFP
GFP-IRSp53
mScarlet-I-Swip1
mScarlet-I-Swip1
Arf1-GFP
mScarlet-I-Swip1
GFP-IRSp53
mScarlet-I-Swip1
e
Colocalization with mScarlet-I-Swip1
% colocalized spots
60
40
20
0
****
****
****
ns
ns
****
Rab21
Clathrin
AP2
Caveolin
GFP-Rab21
GFP-dynamin2
GFP-IRSp53
Arf1-GFP
f
IP
Lysate
Venus
V1-Rab21 +V2-Swip1
KDa
150
75
50
100
50
37
25
β1-integrin
IRSp53
Dynamin I/II
V2-Swip1
V1-Rab21
Venus
g
Time elapsed in movie
101.5 s
102 s
102.5 s
103 s
104 s
104.5 s
V1-Rab21 + V2-Swip1
IRSp53
Merge

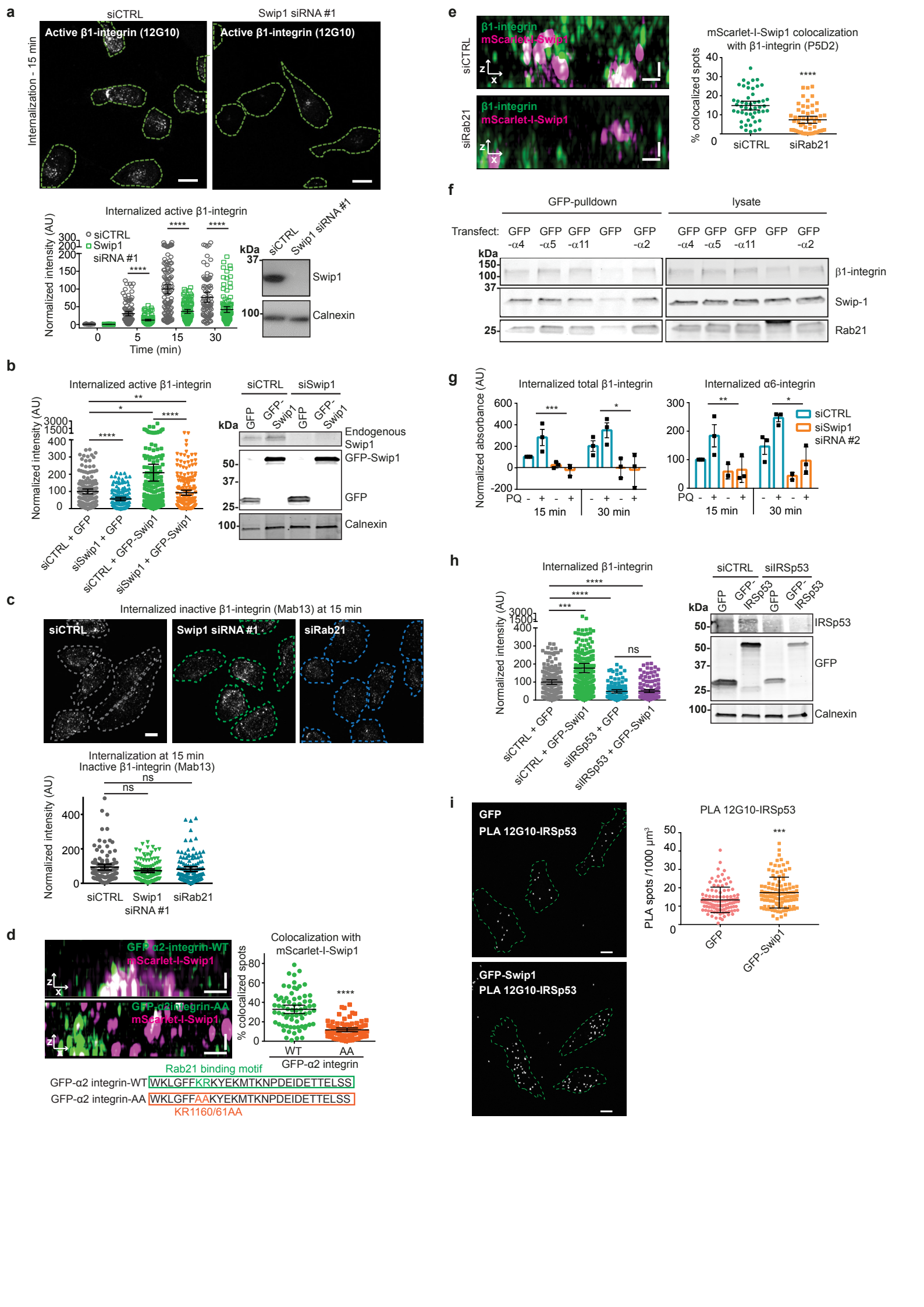
a
siCTRL
Swip1 siRNA #1
Internalization - 15 min
Active β1-integrin (12G10)
Active β1-integrin (12G10)
Internalized active β1-integrin
Normalized intensity (AU)
siCTRL
Swip1 siRNA #1
Time (min)
kDa
siCTRL
Swip1 siRNA #1
Swip1
Calnexin
b
Internalized active β1-integrin
Normalized intensity (AU)
siCTRL + GFP
siSwip1 + GFP
siCTRL + GFP-Swip1
siSwip1 + GFP-Swip1
siCTRL
siSwip1
GFP
GFP-Swip1
kDa
Endogenous Swip1
GFP-Swip1
GFP
Calnexin
c
Internalized inactive β1-integrin (Mab13) at 15 min
siCTRL
Swip1 siRNA #1
siRab21
Internalization at 15 min
Inactive β1-integrin (Mab13)
Normalized intensity (AU)
ns
siCTRL
Swip1 siRNA #1
siRab21
d
GFP-α2-integrin-WT
mScarlet-I-Swip1
GFP-α2-integrin-AA
mScarlet-I-Swip1
Colocalization with mScarlet-I-Swip1
% colocalized spots
WT
AA
GFP-α2 integrin
Rab21 binding motif
GFP-α2 integrin-WT WKLGFFKRKYEKMTKNPDEIDETTELSS
GFP-α2 integrin-AA WKLGFFAAKYEKMTKNPDEIDETTELSS
KR1160/61AA
e
siCTRL
siRab21
β1-integrin
mScarlet-I-Swip1
mScarlet-I-Swip1 colocalization with β1-integrin (P5D2)
% colocalized spots
siCTRL
siRab21
f
GFP-pulldown
lysate
Transfect:
GFP -α4
GFP -α5
GFP -α11
GFP
GFP -α2
kDa
β1-integrin
Swip-1
Rab21
g
Internalized total β1-integrin
Internalized α6-integrin
Normalized absorbance (AU)
PQ
15 min
30 min
siCTRL
siSwip1 siRNA #2
h
Internalized β1-integrin
Normalized intensity (AU)
ns
siCTRL + GFP
siCTRL + GFP-Swip1
siIRSp53 + GFP
siIRSp53 + GFP-Swip1
siCTRL
siIRSp53
GFP
GFP-IRSp53
kDa
IRSp53
GFP
Calnexin
i
GFP
PLA 12G10-IRSp53
GFP-Swip1
PLA 12G10-IRSp53
PLA 12G10-IRSp53
PLA spots /1000 µm³
GFP
GFP-Swip1

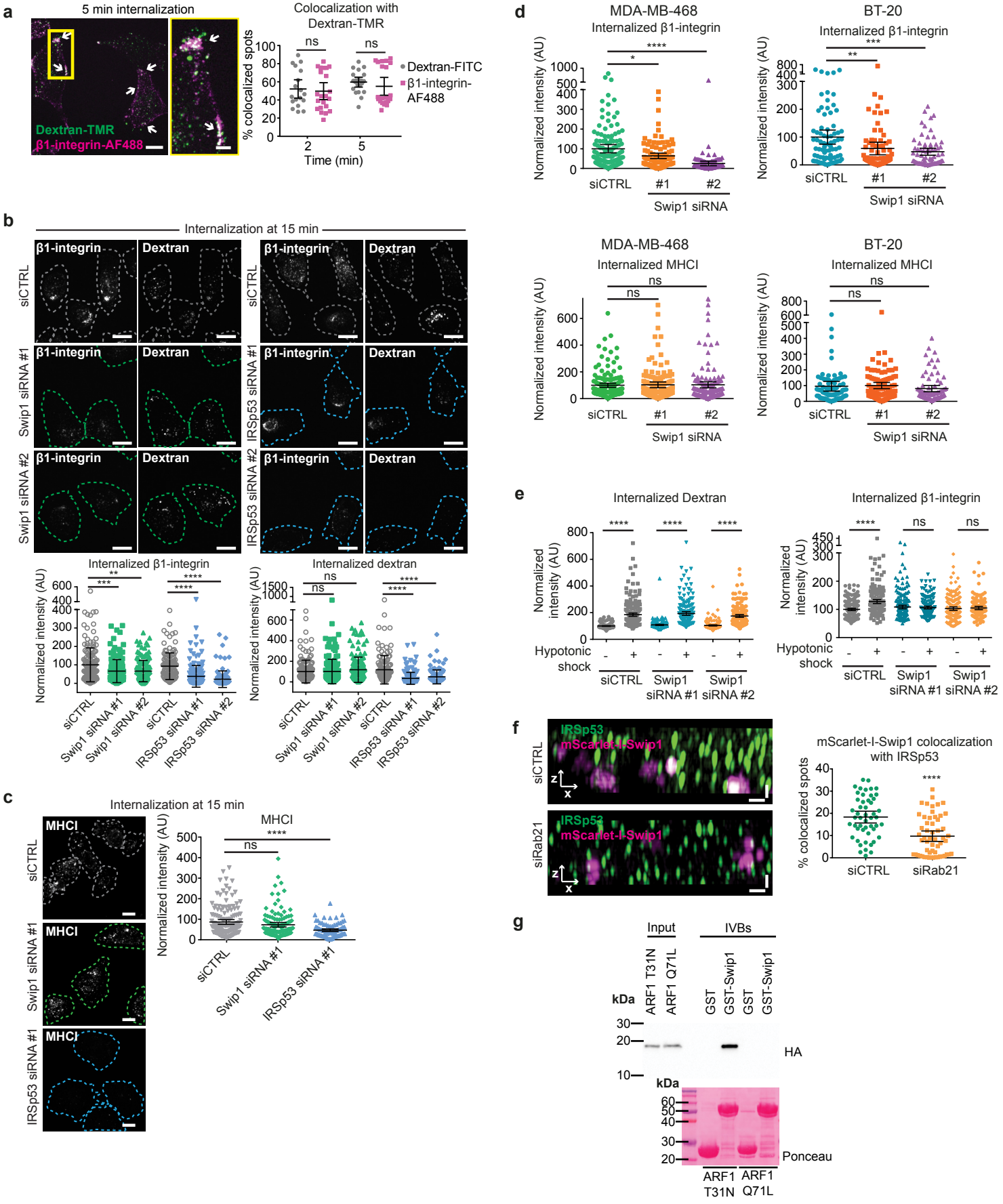
a
5 min internalization
Dextran-TMR
β1-integrin-AF488
Colocalization with Dextran-TMR
% colocalized spots
ns
Dextran-FITC
β1-integrin-AF488
Time (min)
b
Internalization at 15 min
β1-integrin
Dextran
siCTRL
Swip1 siRNA #1
Swip1 siRNA #2
IRSp53 siRNA #1
IRSp53 siRNA #2
Internalized β1-integrin
Internalized dextran
Normalized intensity (AU)
c
Internalization at 15 min
MHCI
Internalized MHCI
d
MDA-MB-468
BT-20
Internalized β1-integrin
Internalized MHCI
Normalized intensity (AU)
Swip1 siRNA
e
Internalized Dextran
Internalized β1-integrin
Normalized intensity (AU)
Hypotonic shock
f
IRSp53
mScarlet-I-Swip1
siRab21
mScarlet-I-Swip1 colocalization with IRSp53
% colocalized spots
g
Input
IVBs
ARF1 T31N
ARF1 Q71L
GST
GST-Swip1
kDa
HA
Ponceau

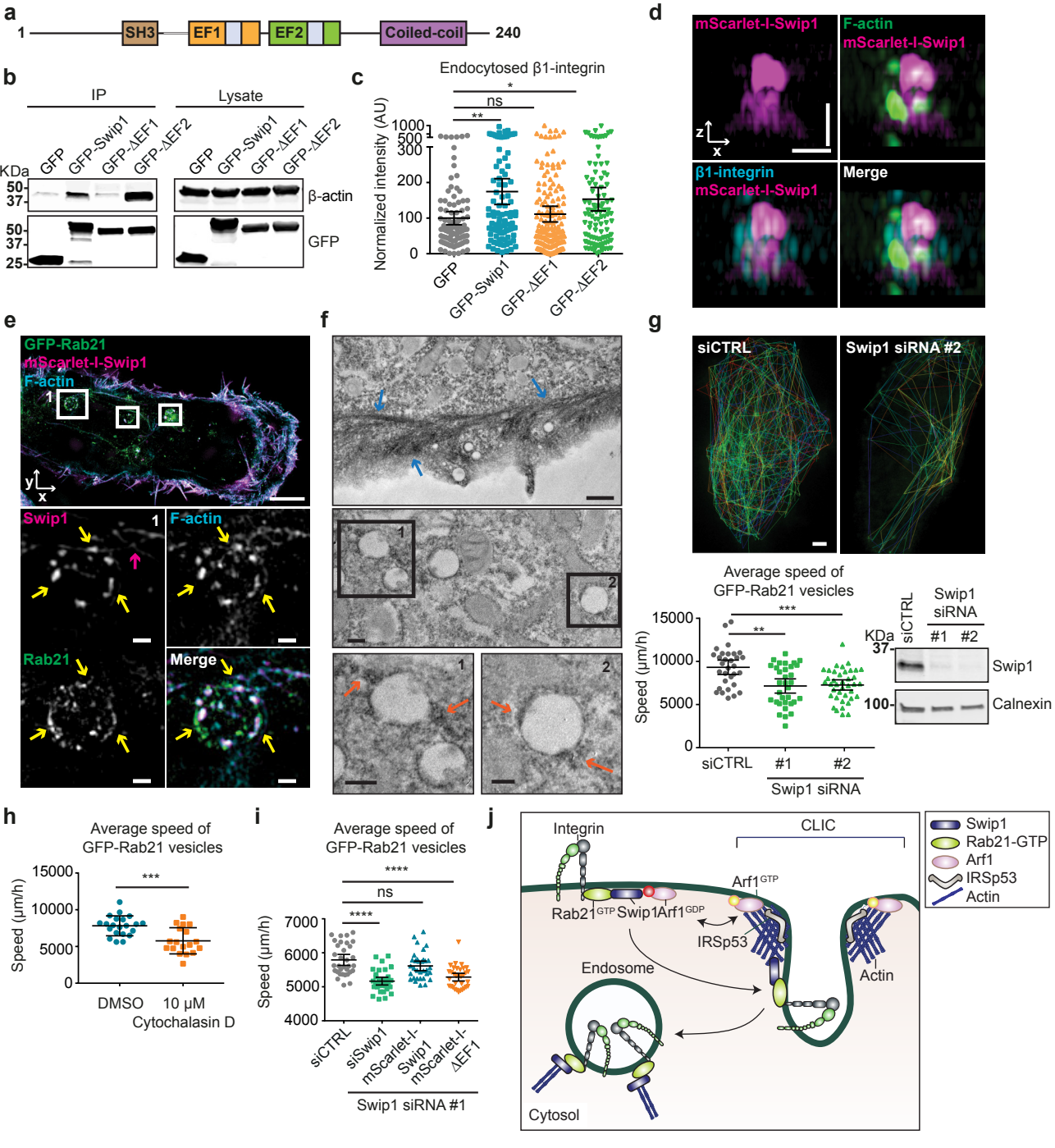
a
1
SH3
EF1
EF2
Coiled-coil
240
b
IP
Lysate
GFP
GFP-Swip1
GFP-ΔEF1
GFP-ΔEF2
KDa
50
37
β-actin
GFP
25
c
Endocytosed β1-integrin
Normalized intensity (AU)
*
ns
**
1000
500
300
200
100
0
d
mScarlet-I-Swip1
F-actin
mScarlet-I-Swip1
z
x
β1-integrin
mScarlet-I-Swip1
Merge
e
GFP-Rab21
mScarlet-I-Swip1
F-actin
1
y
x
Swip1
F-actin
Rab21
Merge
f
1
2
g
siCTRL
Swip1 siRNA #2
Average speed of
GFP-Rab21 vesicles
Speed (μm/h)
15000
10000
5000
0
***
**
siCTRL
#1
#2
Swip1 siRNA
KDa
siCTRL
Swip1 siRNA
#1
#2
37
Swip1
100
Calnexin
h
Average speed of
GFP-Rab21 vesicles
Speed (μm/h)
15000
10000
5000
0
***
DMSO
10 μM
Cytochalasin D
i
Average speed of
GFP-Rab21 vesicles
Speed (μm/h)
7000
6000
5000
4000
****
ns
****
siCTRL
siSwip1
mScarlet-I-Swip1
mScarlet-I-ΔEF1
Swip1 siRNA #1
j
Integrin
CLIC
Arf1GTP
Rab21GTP
Swip1
Arf1GDP
IRSp53
Endosome
Actin
Cytosol
Swip1
Rab21-GTP
Arf1
IRSp53
Actin

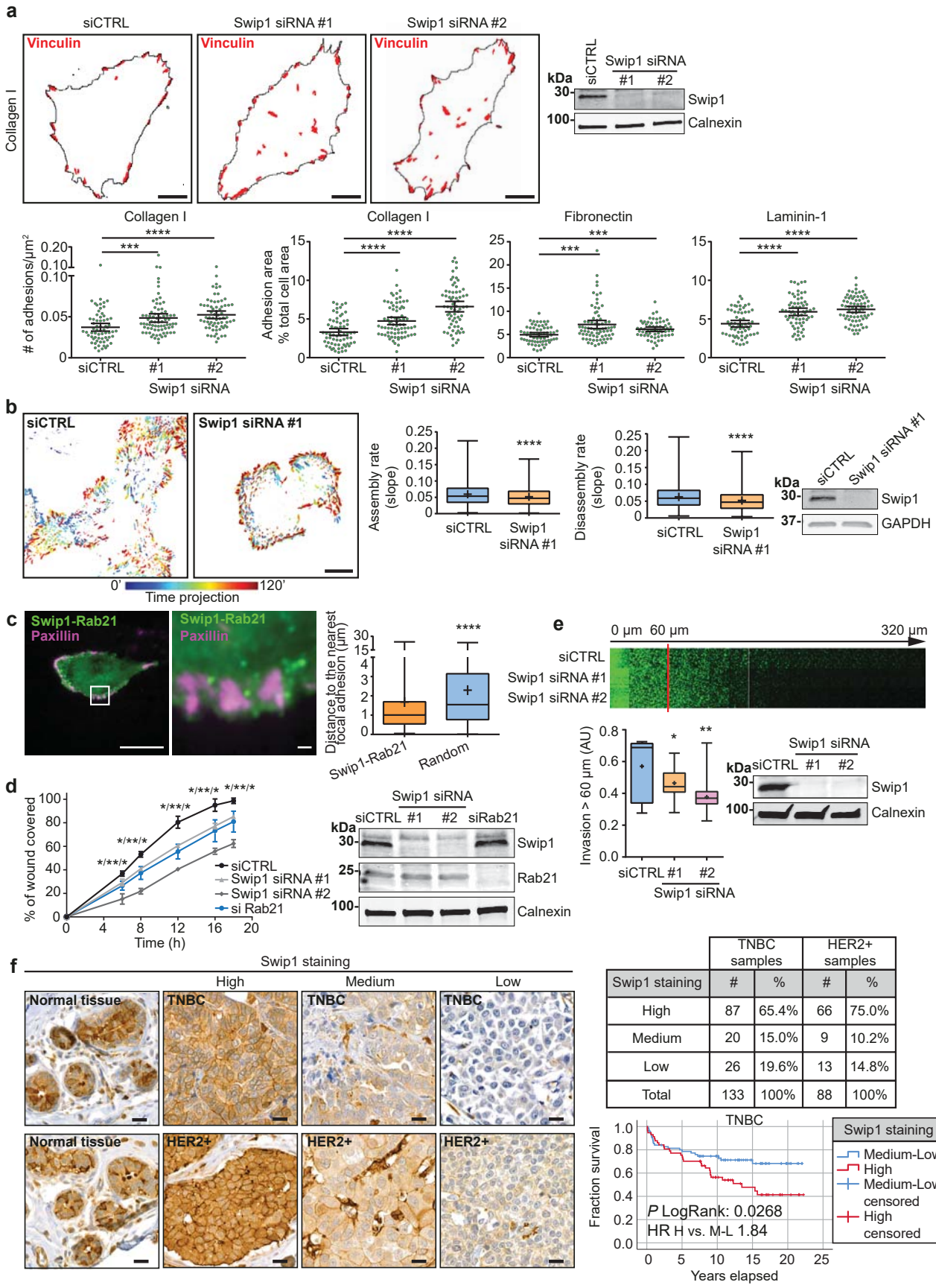

	TNBC samples		HER2+ samples	
Swip1 staining	#	%	#	%
High	87	65.4%	66	75.0%
Medium	20	15.0%	9	10.2%
Low	26	19.6%	13	14.8%
Total	133	100%	88	100%

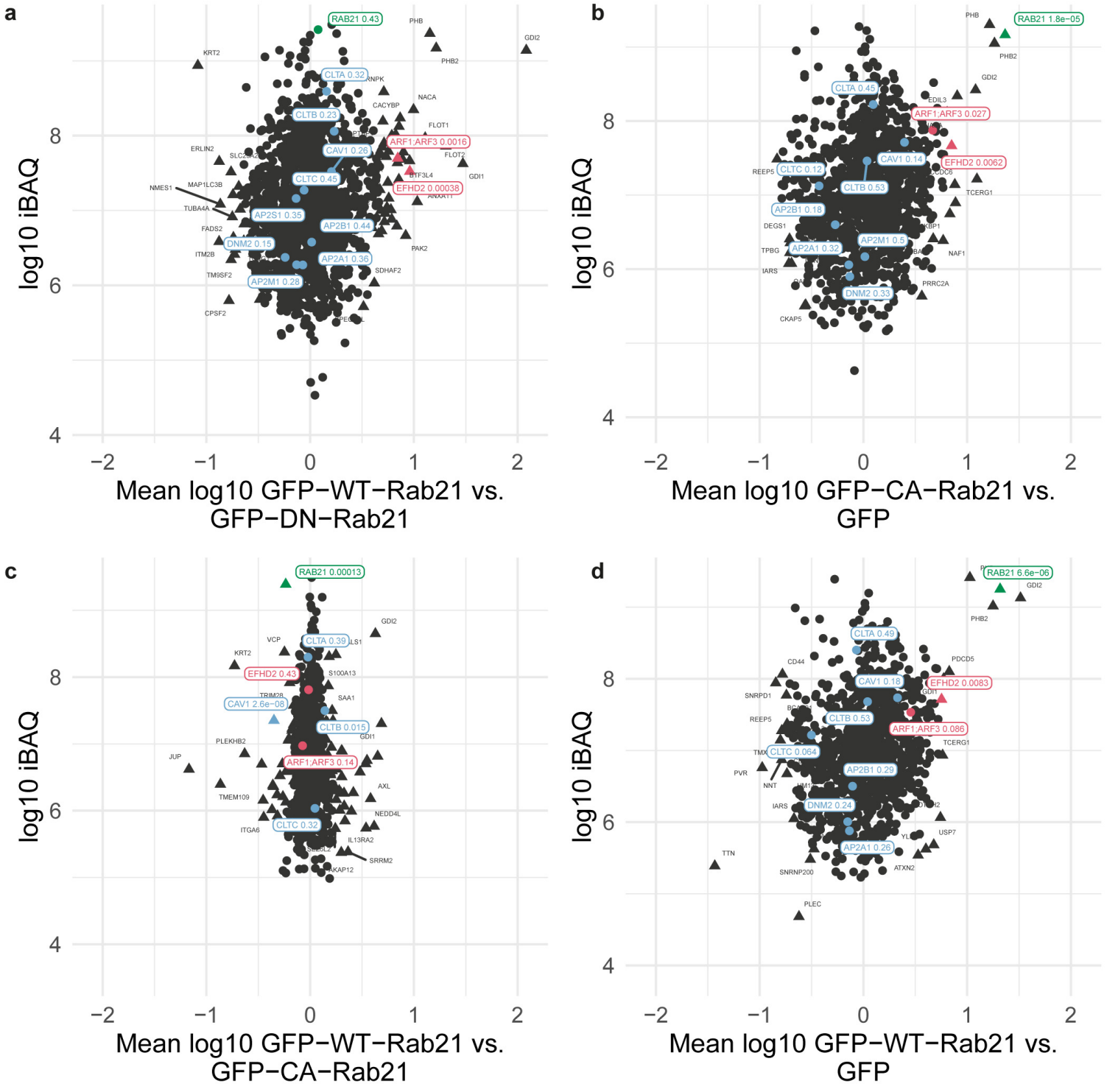
a
log10 iBAQ
Mean log10 GFP−WT−Rab21 vs. GFP−DN−Rab21
RAB21 0.43
CLTA 0.32
CLTB 0.23
CAV1 0.26
CLTC 0.45
AP2S1 0.35
AP2B1 0.44
DNM2 0.15
AP2A1 0.36
AP2M1 0.28
ARF1:ARF3 0.0016
EFHD2 0.00038
b
log10 iBAQ
Mean log10 GFP−CA−Rab21 vs. GFP
RAB21 1.8e−05
CLTA 0.45
CLTC 0.12
CLTB 0.53
AP2B1 0.18
AP2A1 0.32
AP2M1 0.5
DNM2 0.33
ARF1:ARF3 0.027
CAV1 0.14
EFHD2 0.0062
c
log10 iBAQ
Mean log10 GFP−WT−Rab21 vs. GFP−CA−Rab21
RAB21 0.00013
CLTA 0.39
EFHD2 0.43
CAV1 2.6e−08
CLTB 0.015
ARF1:ARF3 0.14
CLTC 0.32
d
log10 iBAQ
Mean log10 GFP−WT−Rab21 vs. GFP
RAB21 6.6e−06
CLTA 0.49
CAV1 0.18
CLTB 0.53
CLTC 0.064
AP2B1 0.29
DNM2 0.24
AP2A1 0.26
EFHD2 0.0083
ARF1:ARF3 0.086
e
IP
Lysate
GFP
GFP-WT-Rab21
GFP-WT-Rab5
GFP-DN-Rab5
GFP-CA-Rab5
kDa
37
100
50
25
Swip1
β1 integrin
GFP

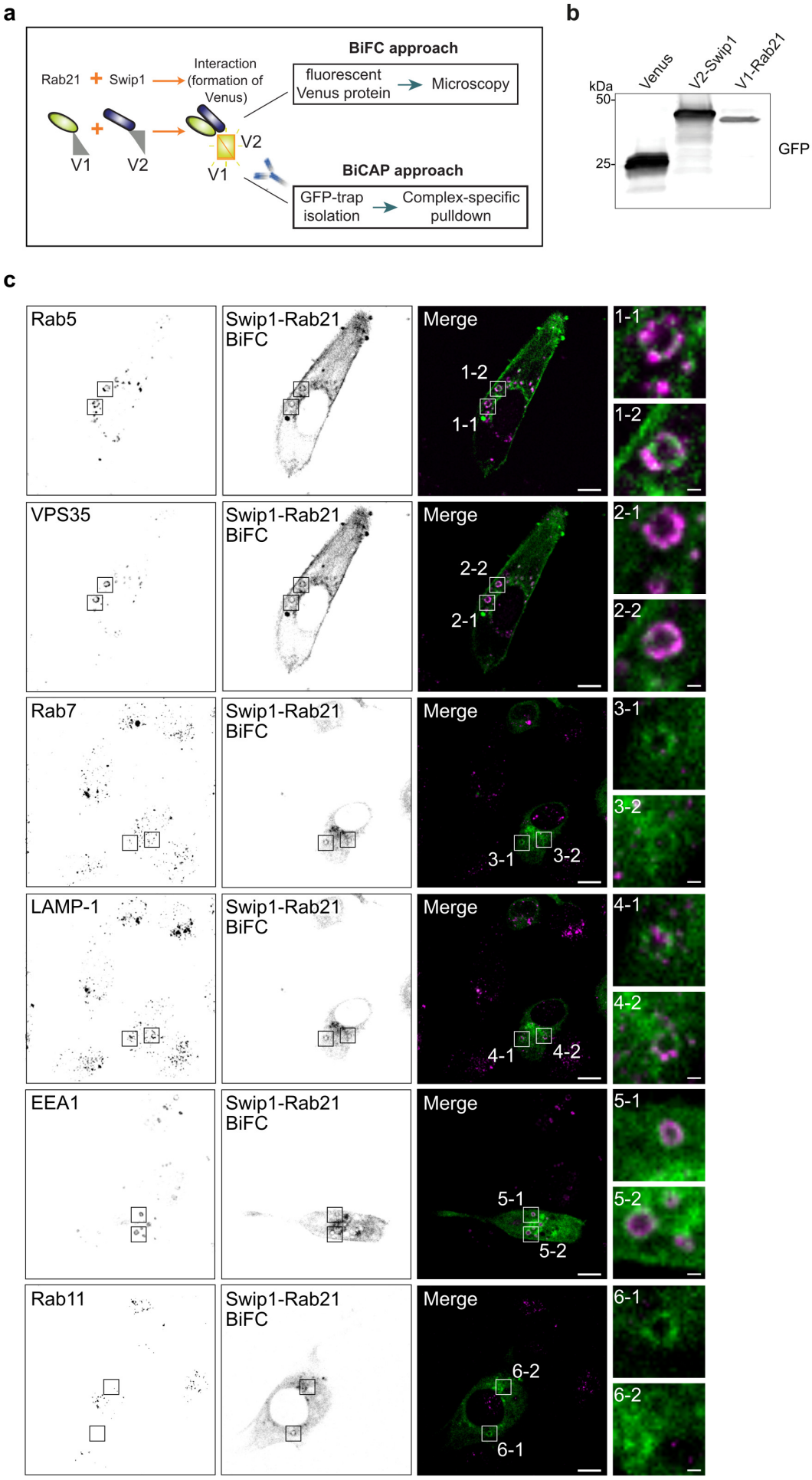
a
BiFC approach
Rab21
Swip1
Interaction
(formation of
Venus)
fluorescent
Venus protein
Microscopy
V1
V2
V2
V1
BiCAP approach
GFP-trap
isolation
Complex-specific
pulldown
b
kDa
Venus
V2-Swip1
V1-Rab21
50-
25-
GFP
c
Rab5
Swip1-Rab21
BiFC
Merge
1-1
1-2
VPS35
2-1
2-2
Rab7
3-1
3-2
LAMP-1
4-1
4-2
EEA1
5-1
5-2
Rab11
6-1
6-2

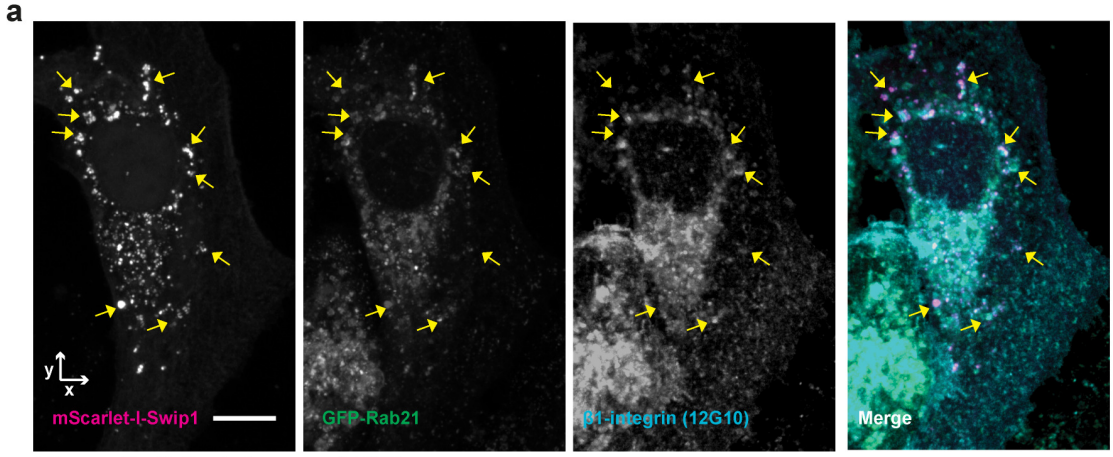

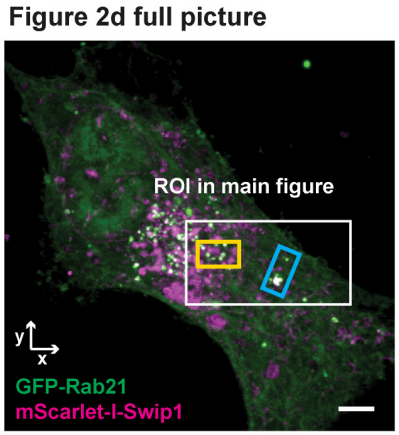

Figure 2e full picture and ROI

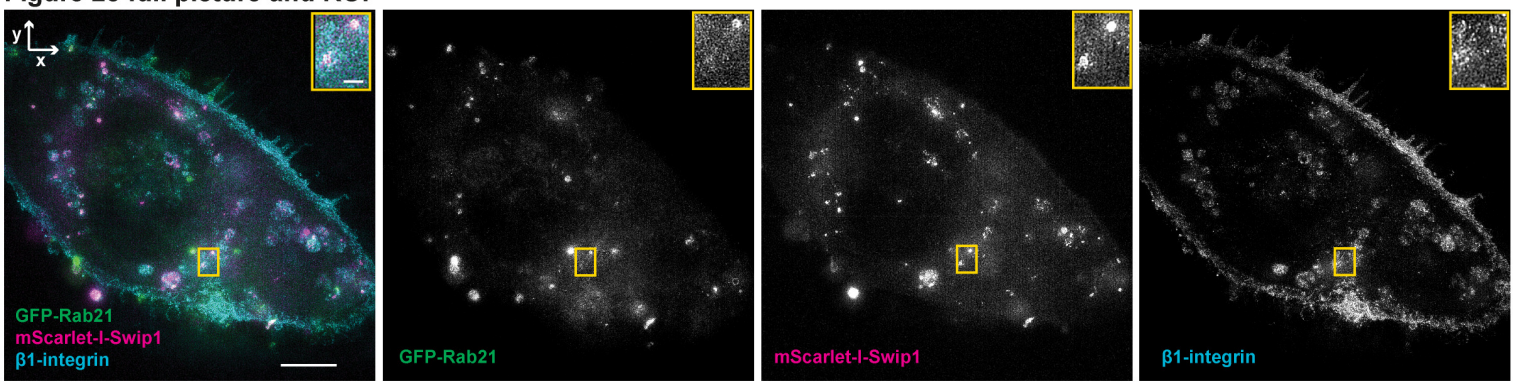

Figure 3d full pictures and ROI

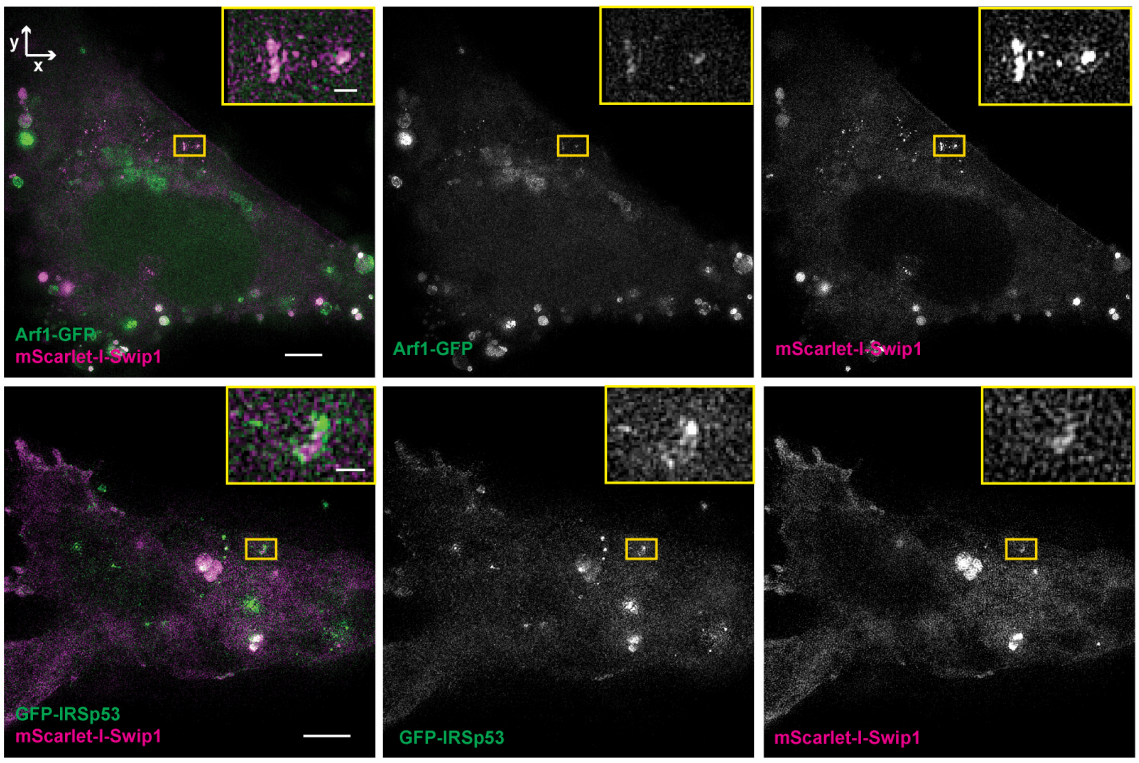

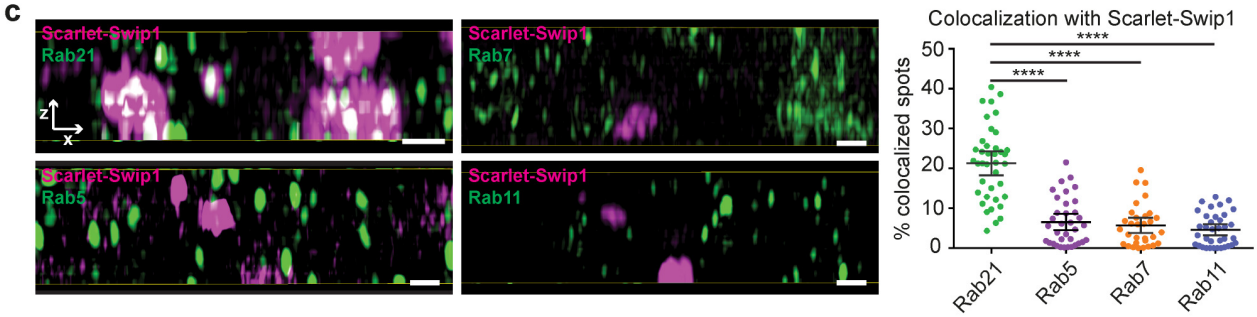

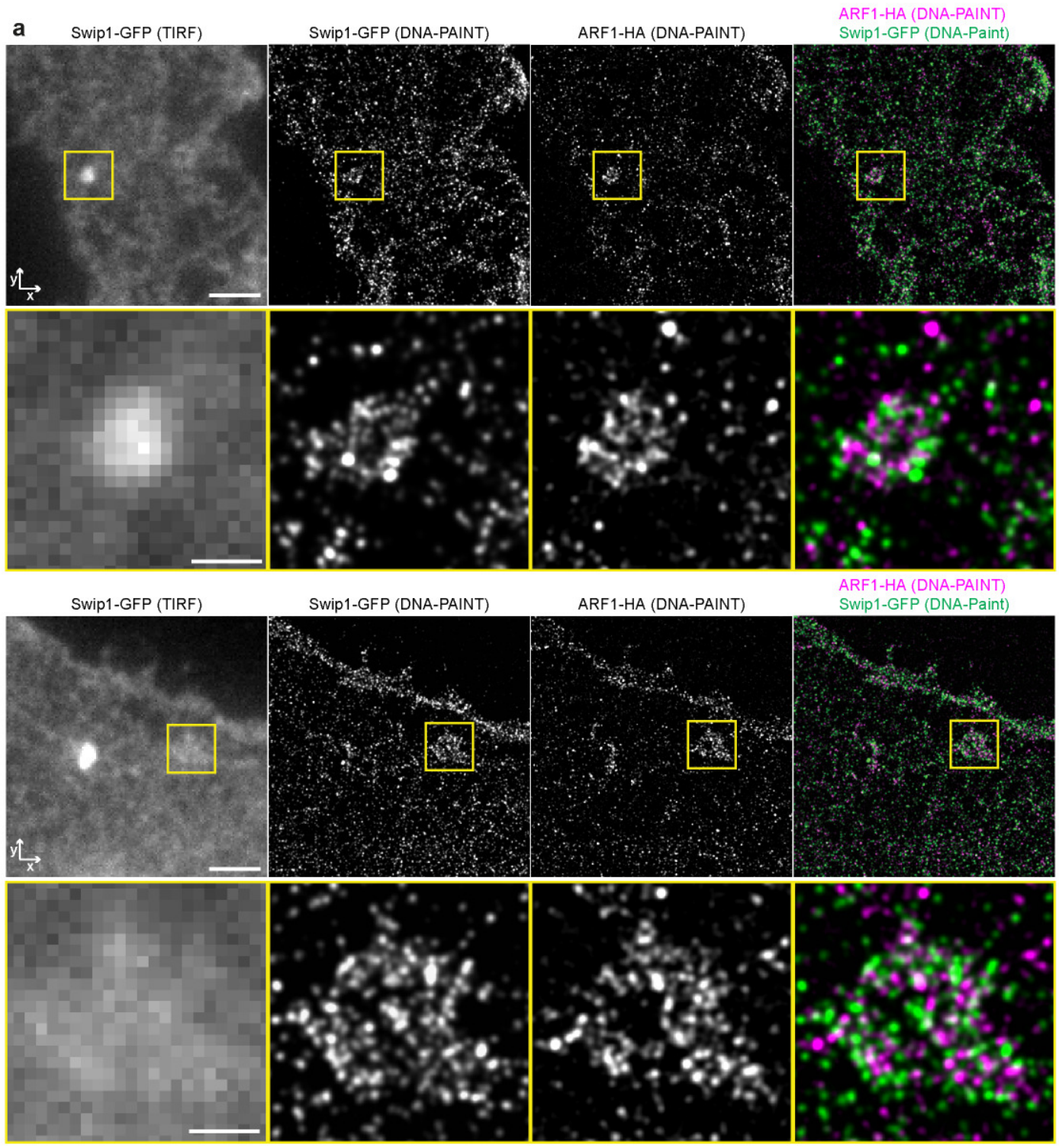
a
Swip1-GFP (TIRF)
Swip1-GFP (DNA-PAINT)
ARF1-HA (DNA-PAINT)
ARF1-HA (DNA-PAINT)
Swip1-GFP (DNA-Paint)
y
x
Swip1-GFP (TIRF)
Swip1-GFP (DNA-PAINT)
ARF1-HA (DNA-PAINT)
ARF1-HA (DNA-PAINT)
Swip1-GFP (DNA-Paint)
y
x

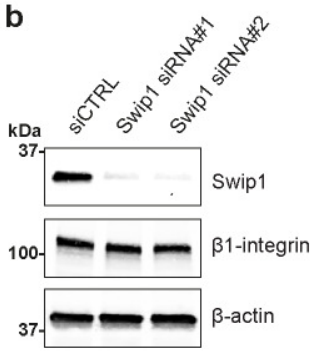
b
siCTRL
Swip1 siRNA#1
Swip1 siRNA#2
kDa
37
Swip1
100
β1-integrin
37
β-actin

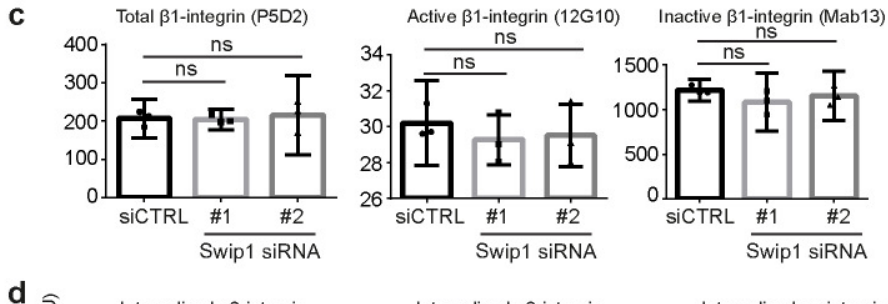
c
Total β1-integrin (P5D2)
400
300
200
100
0
ns
ns
siCTRL
#1
#2
Swip1 siRNA
Active β1-integrin (12G10)
34
32
30
28
26
ns
ns
siCTRL
#1
#2
Swip1 siRNA
Inactive β1-integrin (Mab13)
1500
1000
500
0
ns
ns
siCTRL
#1
#2
Swip1 siRNA

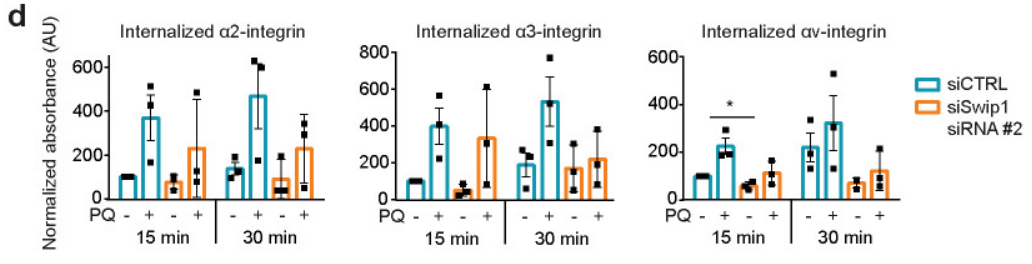
d
Internalized α2-integrin
Normalized absorbance (AU)
600
400
200
0
PQ - + - +
15 min
30 min
Internalized α3-integrin
800
600
400
200
0
PQ - + - +
15 min
30 min
Internalized αv-integrin
600
400
200
0
*
PQ - + - +
15 min
30 min
siCTRL
siSwip1
siRNA #2

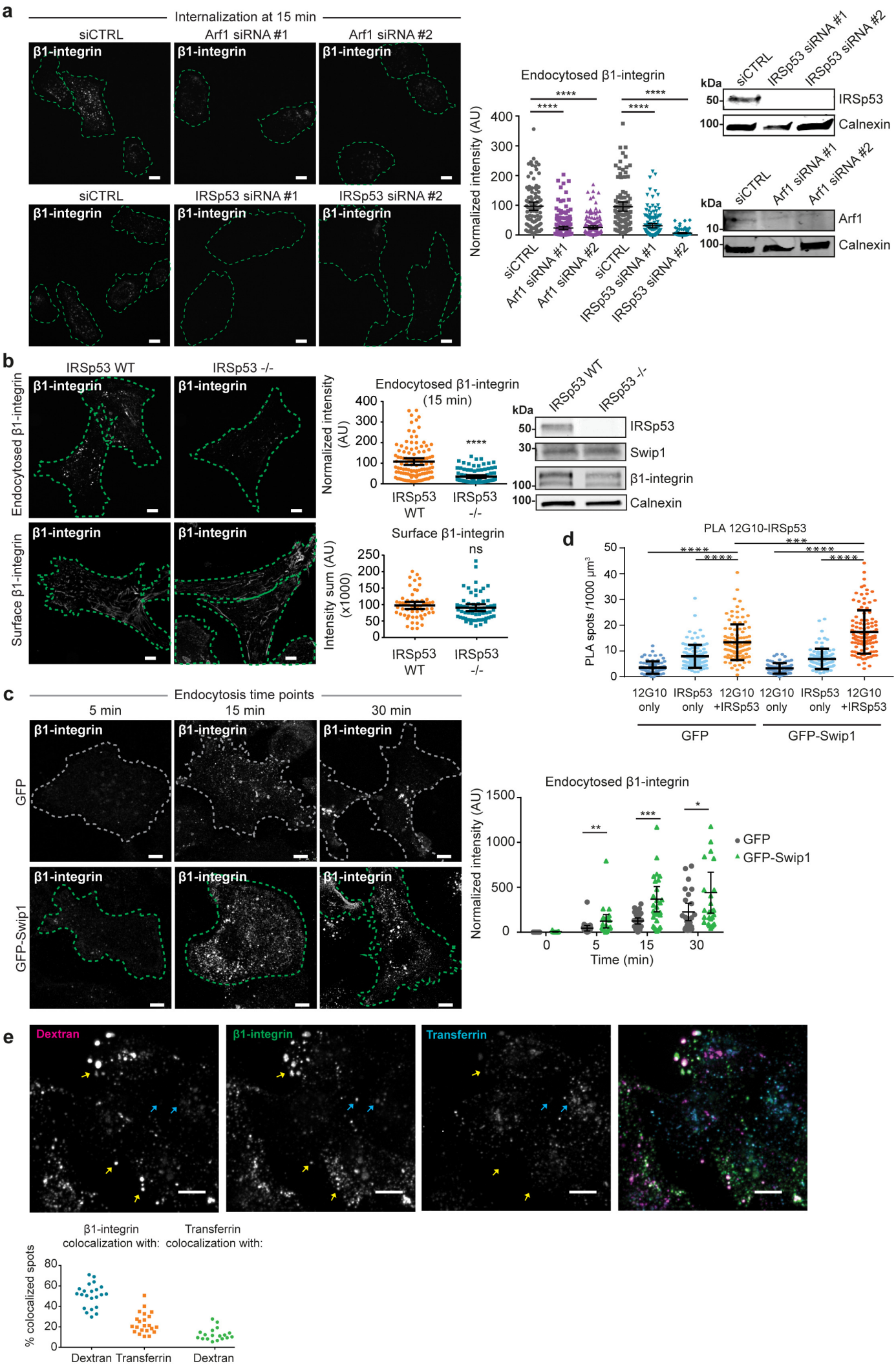
a
Internalization at 15 min
siCTRL
Arf1 siRNA #1
Arf1 siRNA #2
IRSp53 siRNA #1
IRSp53 siRNA #2
β1-integrin
Endocytosed β1-integrin
Normalized intensity (AU)
kDa
IRSp53
Calnexin
Arf1
b
IRSp53 WT
IRSp53 -/-
Endocytosed β1-integrin
Surface β1-integrin
(15 min)
Intensity sum (AU) (x1000)
Swip1
ns
c
Endocytosis time points
5 min
15 min
30 min
GFP
GFP-Swip1
Time (min)
d
PLA 12G10-IRSp53
PLA spots /1000 µm³
12G10 only
IRSp53 only
12G10 +IRSp53
e
Dextran
Transferrin
% colocalized spots
β1-integrin colocalization with:
Transferrin colocalization with:

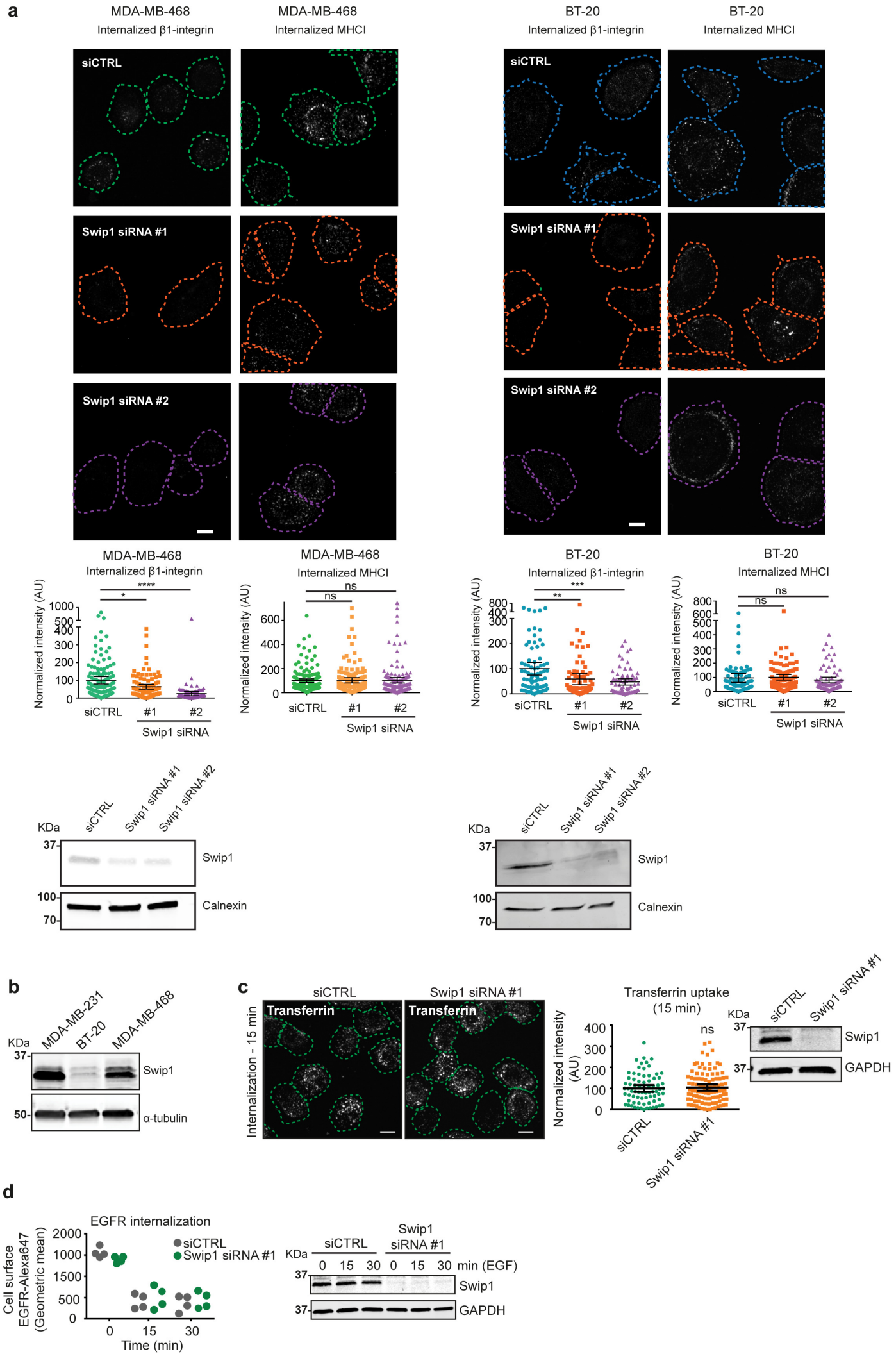
a
MDA-MB-468
Internalized β1-integrin
MDA-MB-468
Internalized MHCI
BT-20
Internalized β1-integrin
BT-20
Internalized MHCI
siCTRL
Swip1 siRNA #1
Swip1 siRNA #2
Normalized intensity (AU)
siCTRL
#1
#2
Swip1 siRNA
ns
KDa
Swip1
Calnexin
b
MDA-MB-231
BT-20
MDA-MB-468
α-tubulin
c
siCTRL
Swip1 siRNA #1
Transferrin
Internalization - 15 min
Transferrin uptake
(15 min)
Normalized intensity
(AU)
GAPDH
d
EGFR internalization
Cell surface
EGFR-Alexa647
(Geometric mean)
Time (min)
Swip1
siRNA #1
min (EGF)

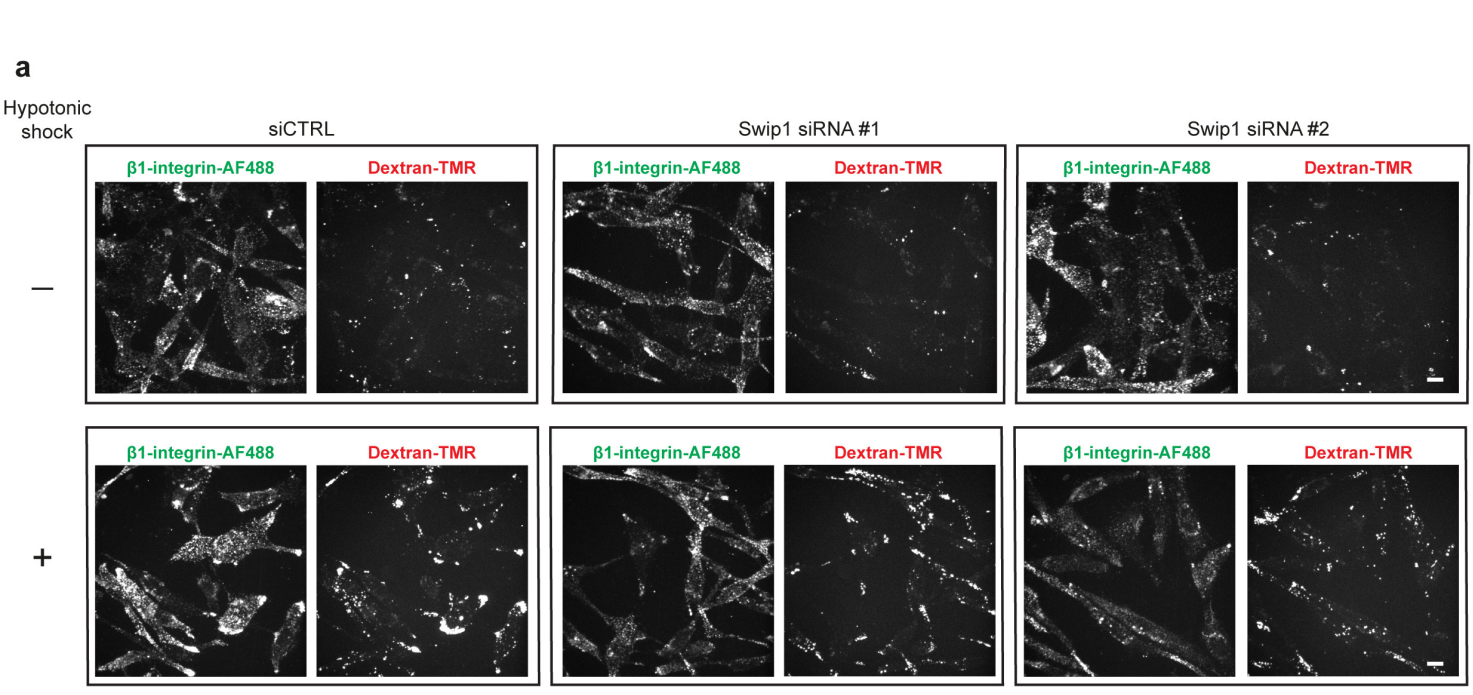
a
Hypotonic shock
siCTRL
Swip1 siRNA #1
Swip1 siRNA #2
β1-integrin-AF488
Dextran-TMR
–
+

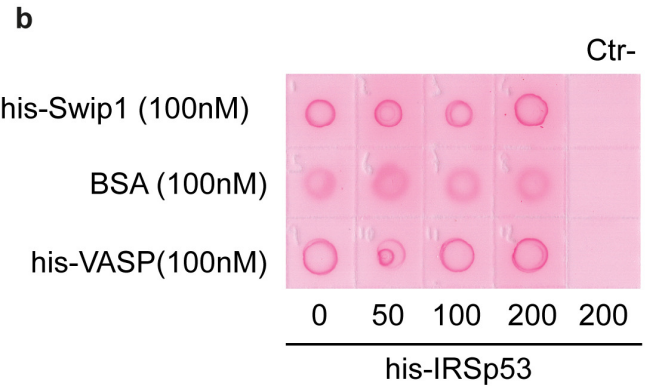
b
Ctr-
his-Swip1 (100nM)
BSA (100nM)
his-VASP(100nM)
0 50 100 200 200
his-IRSp53

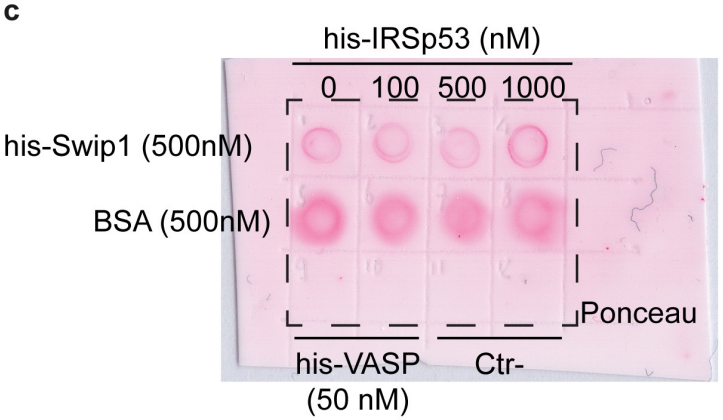
c
his-IRSp53 (nM)
0 100 500 1000
his-Swip1 (500nM)
BSA (500nM)
Ponceau
his-VASP (50 nM)
Ctr-

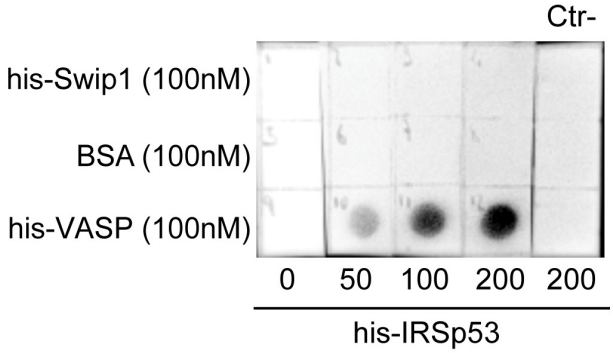
Ctr-
his-Swip1 (100nM)
BSA (100nM)
his-VASP (100nM)
0 50 100 200 200
his-IRSp53

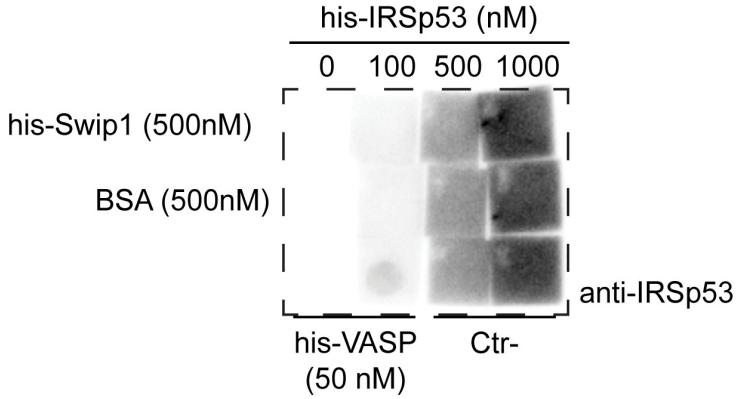
his-IRSp53 (nM)
0 100 500 1000
his-Swip1 (500nM)
BSA (500nM)
anti-IRSp53
his-VASP (50 nM)
Ctr-

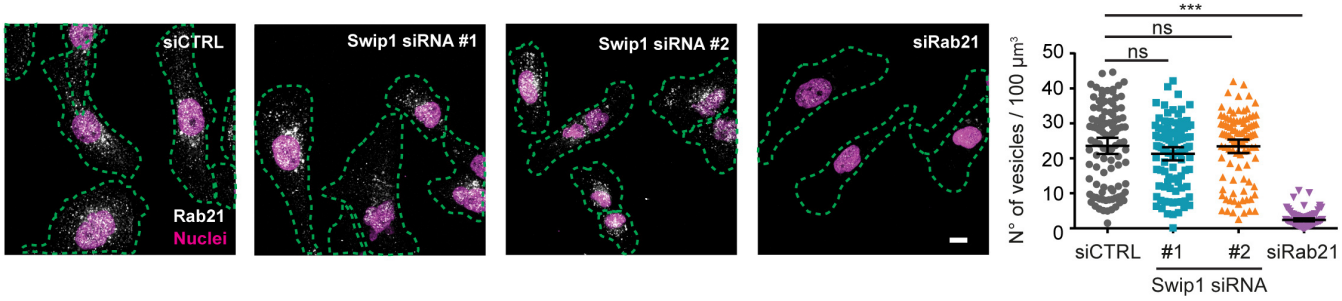
d
siCTRL
Swip1 siRNA #1
Swip1 siRNA #2
siRab21
Rab21
Nuclei
N° of vesicles / 100 µm³
***
ns
ns
siCTRL
#1
#2
siRab21
Swip1 siRNA

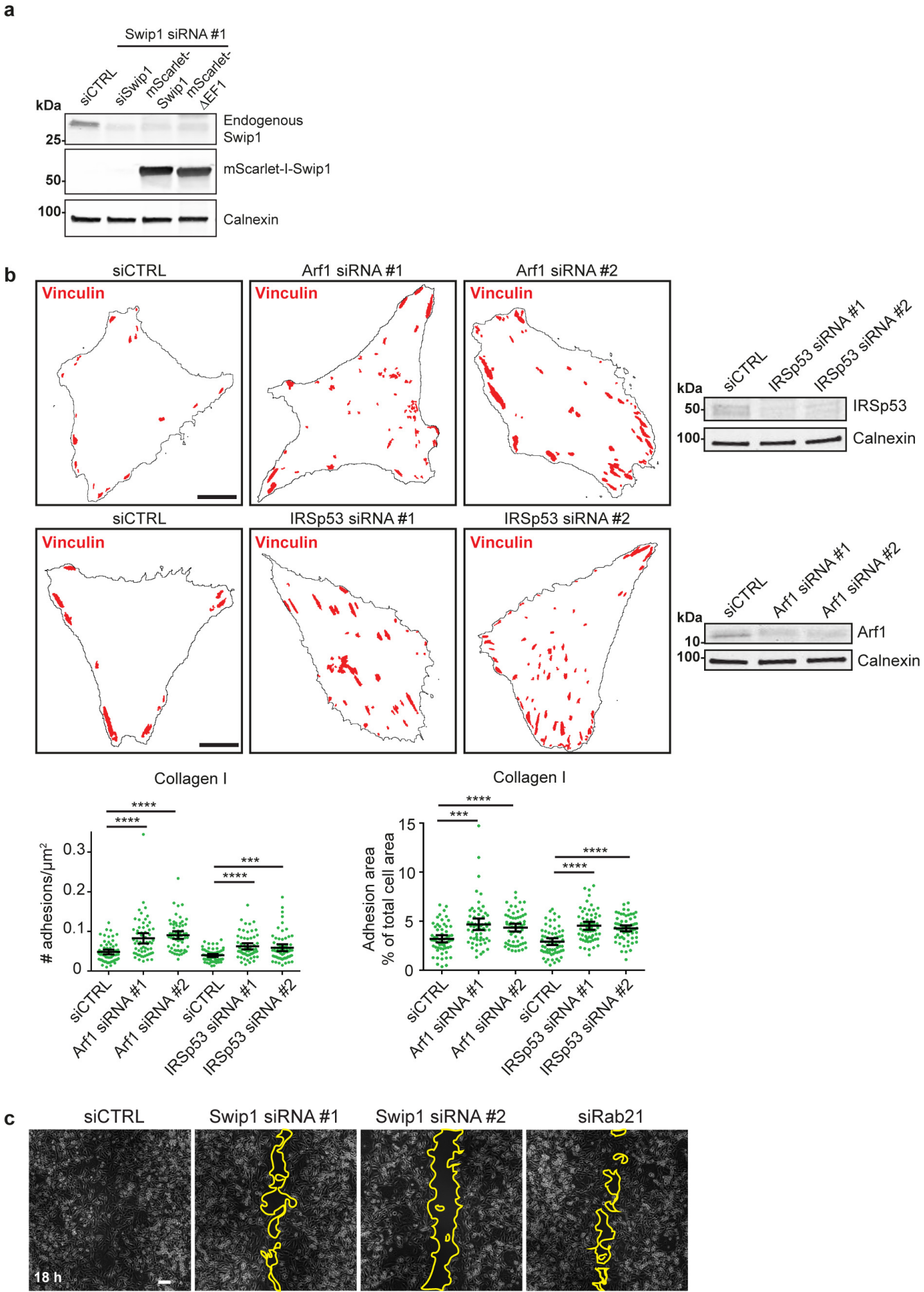
a
Swip1 siRNA #1
siCTRL
siSwip1
mScarlet-Swip1
mScarlet-ΔEF1
kDa
25
50
100
Endogenous Swip1
mScarlet-I-Swip1
Calnexin
b
siCTRL
Arf1 siRNA #1
Arf1 siRNA #2
Vinculin
siCTRL
IRSp53 siRNA #1
IRSp53 siRNA #2
kDa
50
100
IRSp53
Calnexin
siCTRL
Arf1 siRNA #1
Arf1 siRNA #2
kDa
10
100
Arf1
Calnexin
Collagen I
adhesions/µm²
0
0.1
0.2
0.3
****
***
siCTRL
Arf1 siRNA #1
Arf1 siRNA #2
IRSp53 siRNA #1
IRSp53 siRNA #2
Collagen I
Adhesion area % of total cell area
0
5
10
15
c
siCTRL
Swip1 siRNA #1
Swip1 siRNA #2
siRab21
18 h

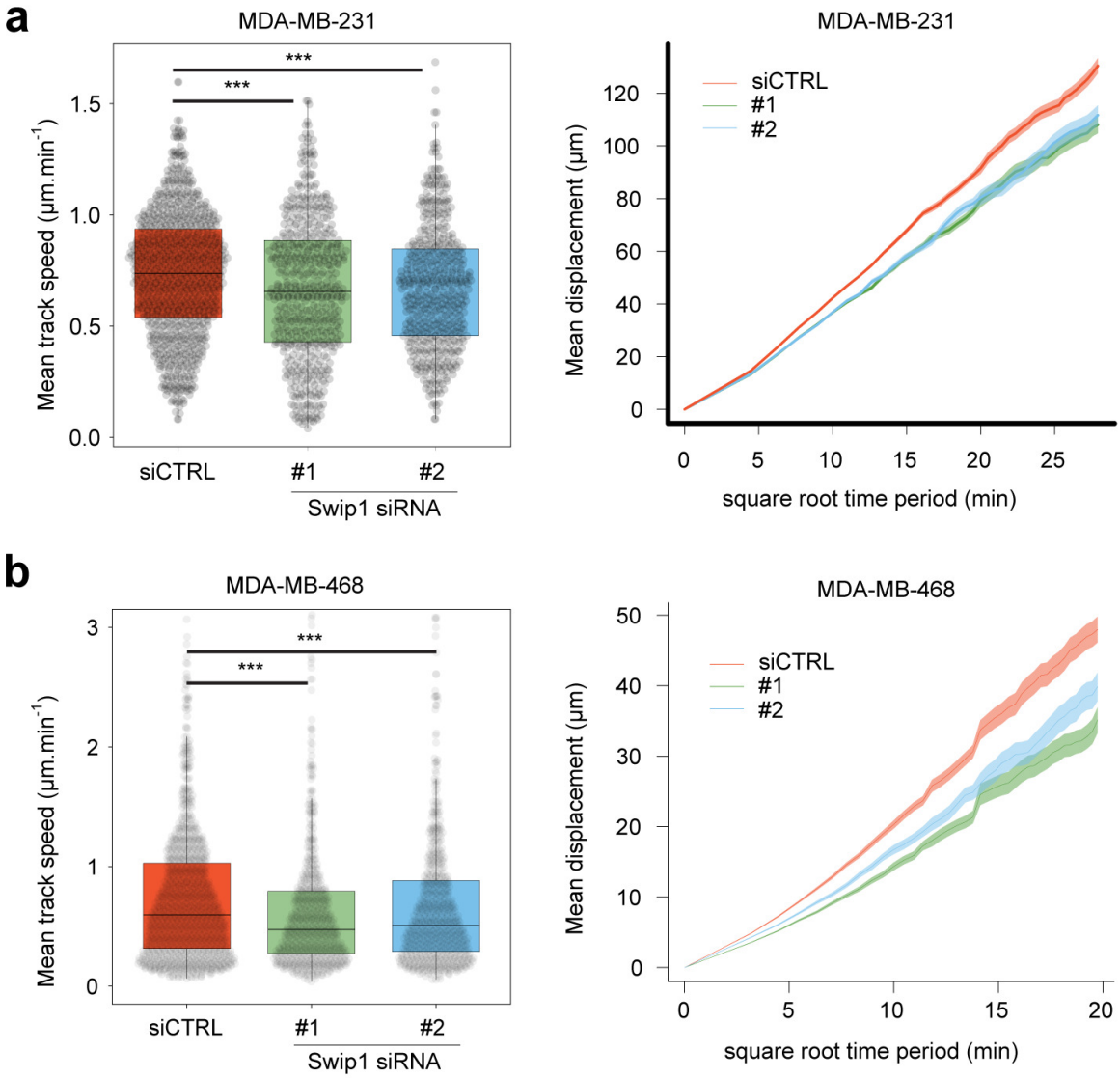
a
MDA-MB-231
***
***
Mean track speed (µm.min-1)
1.5
1.0
0.5
0.0
siCTRL
#1
#2
Swip1 siRNA
MDA-MB-231
siCTRL
#1
#2
Mean displacement (µm)
120
100
80
60
40
20
0
0
5
10
15
20
25
square root time period (min)
b
MDA-MB-468
***
***
Mean track speed (µm.min-1)
3
2
1
0
siCTRL
#1
#2
Swip1 siRNA
MDA-MB-468
siCTRL
#1
#2
Mean displacement (µm)
50
40
30
20
10
0
0
5
10
15
20
square root time period (min)

a

		EFHD2 mRNA level					
		< median		> median		total samples	p
		# samples	% samples	# samples	% samples		
molecular subtype	HER2+	10	34.5%	19	65.5%	29	0.002
	luminal	72	58.5%	51	41.5%	123	
	TNBC	11	29.7%	26	70.3%	37	
total						189	
grading	1	12	60.0%	8	40.0%	20	0.049
	2	47	58.8%	33	41.3%	80	
	3	38	41.3%	54	58.7%	92	
total						192	

b

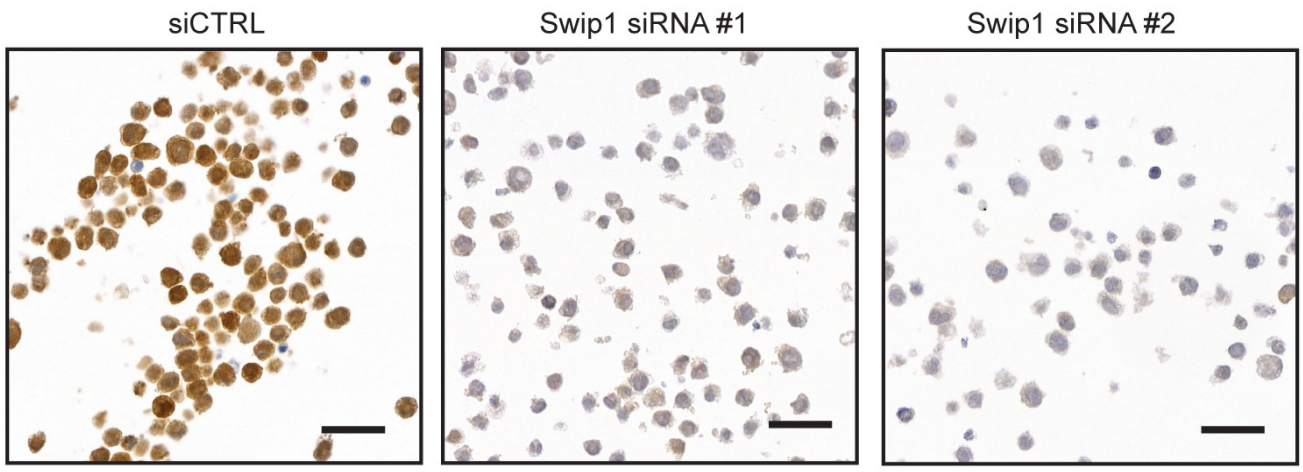

c

	TNBC samples	
Membranal Swip1	#	%
High	20	15.0%
Medium	19	14.3%
Low	94	70.7%
Total	133	100%

d

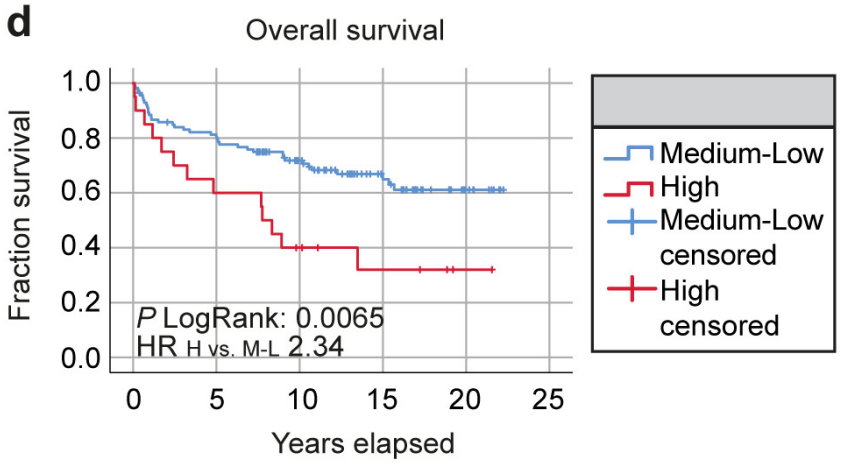

e

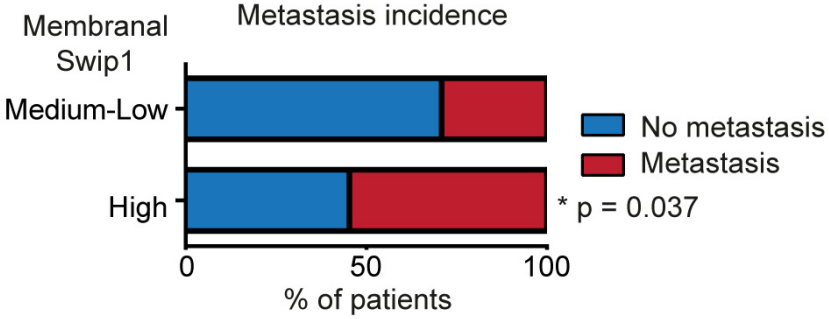

Moreno-Layseca et al., Cargo-specific recruitment in clathrin- and dynamin-independent endocytosis

Supplementary Information:

Supplementary Figure 1. Representative raw flow cytometry data and gating strategy for Extended Data Figure 6d.